

Developing a Machine-Learning Interatomic Potential for Non-Covalent Interactions in Proteins

Lejia Zeng^{1,2}, Xintong Zhang^{1,2}, Yuchan Pei^{1,2}, Lifeng Zhao², Lan Hua², Jincai Yang², Niu Huang^{1,2,}*

¹Tsinghua Institute of Multidisciplinary Biomedical Research, Tsinghua University, Beijing 102206, China

²National Institute of Biological Sciences, 7 Science Park Road, Zhongguancun Life Science Park, Beijing 102206, China

KEYWORDS: Machine Learning Interatomic Potential (MLIP), Non-covalent Interactions (NCI), Active Learning (AL), Quantum Mechanics (QM), Force Field (FF)

* To whom correspondence should be addressed. N. H. (Email) huangniu@nibs.ac.cn (Phone) 86-10-80720645 (Fax) 86-10-80720813

ABSTRACT

Machine learning interatomic potentials (MLIPs) enable efficient modeling of molecular interactions with quantum mechanical (QM) accuracy. However, constructing robust and representative training datasets that capture subtle, system-specific interaction motifs remains challenging. We introduce PANIP (PAirwise Non-covalent Interaction Potential), an ensemble MLIP model built upon the NequIP framework and trained on non-covalent interactions (NCIs) between protein-derived fragments. PANIP is trained using an automated multi-fidelity active learning (MFAL) workflow, in which a representative training subset—termed PDB-FRAGID (PDB Fragment Interaction Dataset), was distilled from an otherwise prohibitively large pool of fragment dimers extracted from the Protein Data Bank (PDB). PANIP retains ω B97X-D3BJ/def2-TZVPP-level accuracy and achieves mean absolute errors below 0.2 kcal/mol on out-of-distribution systems, demonstrating excellent transferability across diverse NCI motifs. Compared to the widely used ANI-2x potential, PANIP delivers substantially lower errors, particularly for charged and strongly interacting dimers. Coupled with a fragmentation-based energy decomposition scheme, PANIP estimates protein–ligand binding energies at near force-field computational cost yet QM-level accuracy, enabling its use as a fragment-based scoring function that rivals specialized docking scoring functions.

INTRODUCTION

The accurate modeling of non-covalent interactions (NCIs) within biomolecules at quantum-mechanical (QM) accuracy remains computationally prohibitive for large systems. The integration of QM methods with machine learning (ML) enables the efficient exploration of complex molecular systems¹⁻³. Machine learning interatomic potentials (MLIPs) reproduce QM potential energy surfaces (PESs) with high fidelity, often achieving QM-level accuracy at a fraction of the computational cost for small- and medium-sized systems. These developments have opened new avenues for efficiently exploring complex conformational and interaction landscapes in chemistry and biology⁴⁻⁷.

However, the reliability and transferability of MLIPs depend critically on the quality, diversity, and balance of the underlying training data. Many existing datasets and MLIP frameworks undersample chemical and conformational spaces⁸⁻¹⁴, emphasize a limited set of molecular species, or are tuned to specific classes of systems, which restricts their applicability to new interaction motifs and environments^{3,5,15-18}. Recent efforts have introduced large-scale, chemically diverse datasets and “universal” models that span broad chemical spaces^{19,20}. However, these primarily emphasize universality, and when it comes to particular and subtle interaction motifs crucial for biological systems, important regions may remain underexplored. In particular, NCIs in proteins involve a rich variety of hydrogen bonding, electrostatic, dispersion, cation- π , and sulfur-containing interactions that are strongly context-dependent and sensitive to local geometry. Capturing these motifs at QM accuracy in a manner that generalizes across diverse protein environments remains a major challenge.

Generating new QM datasets tailored to specific systems or interactions is both labor-intensive and computationally expensive, sometimes negating the gains provided by ML acceleration. Moreover, when such system-specific datasets are integrated with existing large-scale datasets, the amount of additional training data should be carefully controlled to avoid excessive training burden while still filling critical gaps in chemical and conformational coverage. A central challenge is therefore to construct optimized, broadly representative training datasets that minimize redundant QM calculations while maximizing coverage of relevant NCIs. Achieving this goal requires intelligent data selection and model training workflows.

The Protein Data Bank (PDB)²¹ provides a rich, experimentally grounded source of NCI geometries within biologically functional contexts²²⁻²⁵. Unlike synthetic datasets, PDB-derived geometries reflect realistic chemical diversity, spatial complexity, and thermodynamic relevance^{22,23}. This makes the PDB an attractive foundation for building MLIPs that target protein NCIs and are designed to generalize across biologically relevant interaction types, including sidechain-sidechain, sidechain-backbone, and protein-water contacts. At the same time, PDB data exhibits inherent biases, for example, over-representation of certain interactions, resolution limitations, and crystallographic artifacts, which must be carefully considered when constructing datasets and training models.

Leveraging the PDB at scale for MLIP training presents two main challenges. First, generating accurate QM reference energies for the hundreds of millions of possible fragment geometries is computationally prohibitive, even with efficient density functional theory (DFT) methods. Second, the distribution of interaction types in the PDB is highly imbalanced: common interactions such as conventional hydrogen bonds, are heavily over-represented, while rarer but functionally important interactions, including certain cation-π, sulfur-aromatic, or ionic contacts,

occur relatively infrequently. Naively labeling and training on all available dimers would not only be infeasible, but would also risk biasing model learning. Moreover, processing and integrating such a vast structural and energetic dataset during model training requires substantial computational resources and careful data-management strategies.

To address these challenges, a multi-fidelity active learning (MFAL)^{26,27} workflow is employed to construct an efficient, representative dataset and to train an MLIP tailored to protein NCIs. This hierarchical approach integrates low-cost and high-level QM calculations: the composite density functional method r²SCAN-3c²⁸ serves as a low-fidelity oracle for large-scale energetic screening, while a machine learning surrogate identifies a representative and diverse subset for high-level refinement at the ω B97X-D3BJ/def2-TZVPP level^{29,30}. This process yields the PDB Fragment Interaction Dataset (PDB-FRAGID) — a condensed yet representative subset containing only 8.7% of the original pool. Trained on PDB-FRAGID, the resulting ensemble model PANIP achieves accuracy comparable to ω B97X-D3BJ/def2-TZVPP calculations. Built on the Neural Equivariant Interatomic Potentials (NequIP) architecture³¹, PANIP preserves spatial symmetries and accurately captures atomic environments. The model was rigorously validated against multiple benchmark sets, including low-energy dimers, optimized dimers, geometries from the Cambridge Structural Database (CSD)³², and non-equilibrium conformations generated by random sampling. Using this framework, we systematically characterized NCI patterns across the entire PDB, with particular emphasis on underexplored sulfur-driven interactions. Finally, we demonstrate PANIP’s potential utility by applying it as a fragment-based³³ scoring function for protein-ligand binding prediction in benchmark systems.

RESULTS

PDB-FRAGID Dataset Construction. A major challenge in developing MLIPs is constructing training sets that simultaneously provide broad coverage of chemically diverse NCIs and remain computationally tractable for high-level QM labeling. To address this, an iterative data selection strategy using MFAL was used to reduce the initial 36.3 million PDB-derived dimers into a compact, information-rich dataset, PDB-FRAGID. Using r^2 SCAN-3c as a low-fidelity oracle, interaction energies were computed for all dimers, and a NequIP-based surrogate model was iteratively refined to identify high-error dimers for inclusion. This process distilled the dataset to approximately 3.15 million dimers (8.7% of the original pool, Figure 1, Table S1), while preserving coverage across 17 fragment types and 153 dimer combinations and prioritizing chemically challenging systems such as charged and polar fragments (Figure 1). Although r^2 SCAN-3c provides a cost-effective baseline and correlates strongly with ω B97X-D3BJ (Figure S8), it shows systematic deviations for certain noncovalent interactions, including π -stacking and ionic contacts (RMSE=0.423 kcal/mol). Therefore, ω B97X-D3BJ/def2-TZVPP calculations were used to generate the final energy labels.

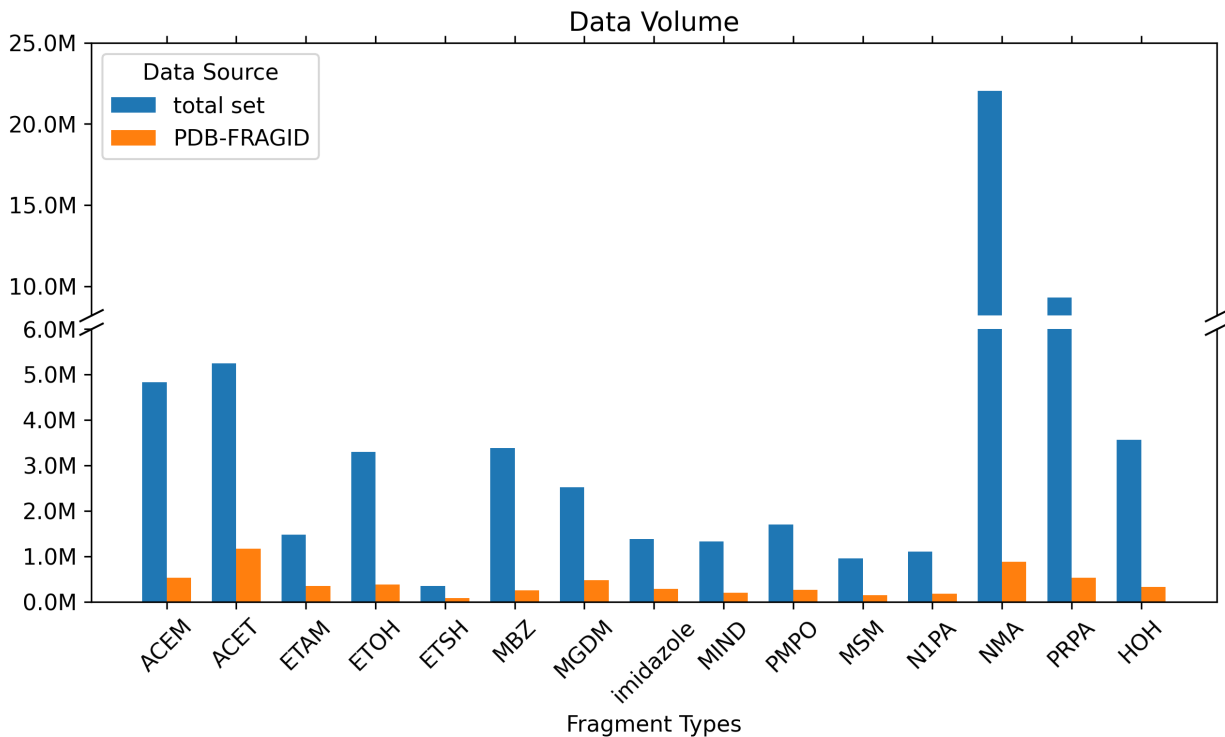


Figure 1. Data Volume for each fragment.

Model Performance on Benchmark Sets. PANIP was evaluated on four benchmark sets to assess accuracy, robustness, and transferability: low-energy dimers, optimized low-energy dimers, CSD-derived geometries, and non-equilibrium conformations generated by biased random sampling (Figure 2). For the PDB-derived low-energy dimers, PANIP achieved a mean absolute error (MAE) of 0.09 kcal/mol, a root mean squared error (RMSE) of 0.163 kcal/mol, and an $R^2=0.999$ relative to ω B97X-D3BJ/def2-TZVPP, indicating excellent reproduction of equilibrium NCI energies in the training domain (Figure 2A). After geometry optimization, the MAE and RMSE increased to 0.547 and 1.207 kcal/mol, respectively, but remained within chemically acceptable limits, indicating that the model can capture the energetic landscape near the equilibrium structures (Figure 2B).

On the CSD-derived benchmark set, which probes transferability to small-molecule crystal environments distinct from proteins, PANIP maintained strong performance (MAE 0.171

kcal/mol, RMSE 0.507 kcal/mol, $R^2=0.999$; Figure 2C), underscoring its generalization beyond PDB geometries. For 15,300 randomly sampled conformations, PANIP achieved an overall MAE of 0.448 kcal/mol, RMSE of 1.372 kcal/mol, and $R^2=0.996$. When restricted to physically plausible dimers (8,572 entries with interaction energy < 0 kcal/mol), the MAE and RMSE improved to 0.195 and 0.363 kcal/mol, respectively, with $R^2=0.999$ (Figure S4a). The subset with interaction energies above 0 kcal/mol (6,728 entries) showed a relatively higher error (RMSE 0.882 kcal/mol; Figure S4b). High-energy outliers (> 100 kcal/mol), representing less than 5% of the dataset, were systematically underestimated due to severe steric clashes and limited training analogs (e.g., ETSH dimers; Figure 1), but these geometries are rare in realistic biomolecular applications.

Computationally, PANIP delivers more than two orders-of-magnitude speedups over direct QM calculations. For example, evaluating 15,300 randomly generated samples on a single CPU core, ω B97X-D3BJ/def2-TZVPP calculations would require 463 days and 11 hours, whereas PNAIP predictions completed in just 6 hours and 11 minutes, reflecting near-linear scaling compared to the formal N^4 scaling of hybrid DFT methods (cubic with modern RI/RIJCOSX implementations; Table S2)²⁹.

Considering that NCIs are diverse and highly sensitive to subtle structural variations, even minor conformational changes can lead to pronounced energy differences^{34,35}. The model's success in predicting unseen conformations underscores the sufficiency of PDB-derived dimers in sampling conformational space, enabling reliable generalization—a critical challenge in developing MLIPs. This emphasizes the importance of representative training sets for capturing diverse conformational and interaction landscapes. Such capabilities are particularly vital for

applications in drug discovery and protein engineering, where accurate prediction of NCIs is essential.

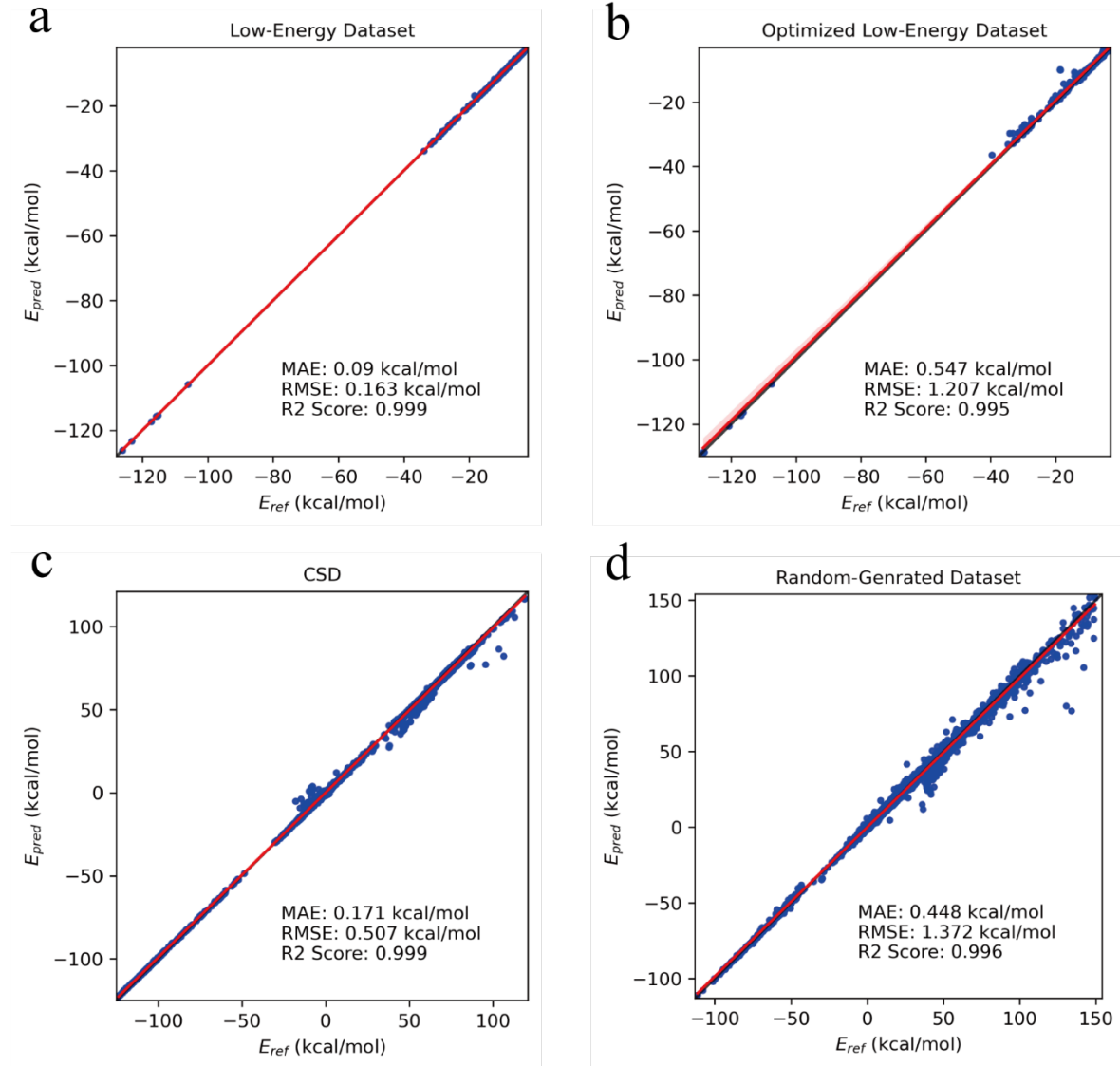


Figure 2. Correlation plots between non-covalent interaction energies calculated at ω B97X-D3BJ/def2-TZVPP level, E_{ref} , and predicted by PANIP, E_{pred} , for the low-energy dataset (a), optimized low-energy dataset (b), CSD subset (c), and random-generated dataset (d). The black line indicates perfect prediction ($y=x$), and the red line shows the regression fit.

Comparison with ANI-2x. Benchmarking against ANI-2x on the CSD-derived geometries (Figure 3a, b) and the other three benchmark sets (Figure S5) highlights PANIP’s superior performance. On the full CSD subset, ANI-2x exhibited large errors (MAE 9.261 kcal/mol, RMSE 23.765 kcal/mol, $R^2=0.064$), with systematic overestimation of strongly attractive dimers (interaction energies < -40 kcal/mol) and underestimation of strongly repulsive dimers (> 40 kcal/mol), particularly in the presence of charged species (e.g., ACET–ETAM, ACET–ACET). These deviations likely stem from the absence of charged species in the ANI-2x’s training data and the indirect computation of interaction energies as differences of total energies without explicit BSSE correction³⁶. Even after excluding dimers containing charged fragments, ANI-2x remained less accurate (MAE 0.882 kcal/mol, RMSE 1.25 kcal/mol, $R^2 = 0.846$; Figure 3b), and similar performance limitations were observed across additional benchmark sets, where MAEs typically exceeded 1 kcal/mol (Figure S5). In contrast, PANIP directly predicts high-level NCI energies, avoids compounded errors from total energy differences, and consistently achieves sub-chemical-accuracy MAEs, including for charged and strongly interacting dimers. These results highlight the importance of high-fidelity NCI training data and a protein-specific design for accurate modeling of biomolecular NCIs.

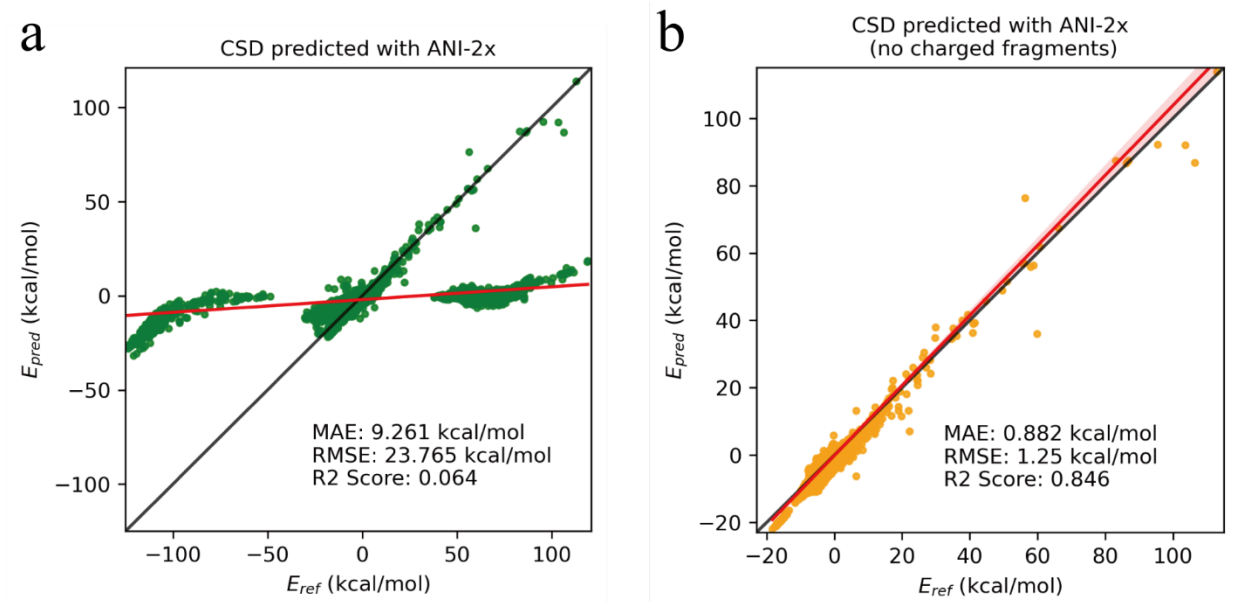


Figure 3. Correlation plots between non-covalent interaction energies calculated at ω B97X-D3BJ/def2-TZVPP level, E_{ref} , and predicted by ANI-2x, E_{pred} , for the CSD-derived benchmark set: (a) all samples; (b) excluding dimers containing charged fragments. The black line indicates perfect prediction ($y=x$), and the red line shows the regression fit.

Exploring NCI Patterns in the PDB. Leveraging PANIP's accuracy and efficiency, the interaction energies were predicted for all 36.3 million PDB-derived dimers, enabling systematic mapping of energy-geometry correlations across the entire dataset (Figure 4, Figure S6). Representative analyses focus on both well-characterized interactions like cation- π interactions, and previously underexplored interactions like dimethyl sulfide–aromatic contacts, to illustrate the model's ability to recover known patterns and reveal new trends. The lowest-energy representative conformations were selected for each interaction pattern and their NCI maps³⁷ were visualized to highlight regions where weak interactions predominantly occur, a detailed description of the NCI visualization method is provided in the Supporting Information.

For Cation- π Interaction, dimers involving lysine (ETAM) with tyrosine (PMPO) or tryptophan (MIND) were examined, yielding 28,914 unique ETAM-PMPO and 24,098 ETAM-MIND dimers. Spatial distribution of the cation relative to the aromatic ring revealed distinct low-energy geometries with centroid distances varying from 4.5 to 7 Å. Positively charged ETAM monomers are predominantly localized around the phenolic hydroxyl group of PMPO, forming a ring-shaped low-energy region, as well as another low-energy region above the aromatic π ring (Figure 4a and Figure S6a). Three representative conformations were identified. *Struc_1* with the lowest-energy (-20.41 kcal/mol) features ETAM simultaneously engaging in a cation- π interaction (N atom 2.9 Å from the phenol ring center) and a nonclassical hydrogen bond between the methyl group of ETAM and the hydroxyl group of PMPO. Cation- π interaction dimers accounted for 17.7% of ETAM-PMPO dimers. *Struc_2* (-19.52 kcal/mol) is dominated by a strong NH \cdots O hydrogen bond between ETAM's NH group and PMPO's hydroxyl oxygen, with a prevalence of 19.8%. The conformation involving a CH \cdots π interaction between the methylene groups of ETAM and the aromatic ring of PMPO is less frequent and higher in energy (Figures 4a, *struc_3*).

Due to the enhanced electron density on Trp's six-membered ring, ETAM tends to interact with MIND above this ring (Figure S6b), with centroid distances of 5-6.5 Å. Figure 4b shows the lowest-energy structures of three representative NCI patterns. The lowest-energy structure, *struc_1* (-24.22 kcal/mol), involves a strong cation- π interaction between ETAM's nitrogen atom and the indole ring. Cation- π interaction dimers accounted for 27.6% of ETAM-MIND dimers. Conformation represented by *struc_2* (-15.44 kcal/mol) adopts a "parallel" orientation between ETAM heavy-atom plane and the indole ring, in which hydrogens attached to the three heavy atoms form weak XH \cdots π interactions with the aromatic ring simultaneously. In contrast, *struc_3*

(-10.83 kcal/mol) features a perpendicular arrangement dominated by methylene CH \cdots π interactions accounting for 33.7% of dimers. These findings align with prior studies³⁸⁻⁴², supporting the reliability of PANIP for large-scale NCI analysis.

For previously underexplored dimethyl sulfide–aromatic Interactions^{43,44}, 78,674 MSM (methionine)–MBZ (phenylalanine) dimers were extracted and analyzed. These revealed five distinct low-energy geometric patterns (Figure 4c, Figure S6c, and Figure S7), spanning interaction distances of 3.5–7 Å with a predominant peak near 5.1 Å and interaction energies ranging from -4.9 to 0.2 kcal/mol (most populated around -1.6 kcal/mol). Mapping the sulfur positions shows that low-energy structures (~ -4 kcal/mol) concentrate in a previously unreported ring-shaped region above the aromatic plane, reflecting stereochemical preferences of sulfur and complementary electrostatic interactions (Figure S6c). Joint analysis of energetic and orientational preferences identifies five low-energy patterns. In the innermost region, C–S bond points toward the ring (Figure S7a), consistent with stereochemical preferences of divalent sulfur approaching the positively polarized aromatic edge (Figure 4c, *struc_5*, -1.52 kcal/mol). Parallel arrangements, in which both the C–S bond and the MSM plane align parallel to the aromatic ring (Figure S7b and S7c), yield the lowest energy (*struc_1*, -4.91 kcal/mol) through complementary electrostatic interactions between sulfur and methyl dipoles. When positioned farther from the aromatic ring, MSM assumes an outward-pointing C–S bond geometry (Figure S7a; *struc_4*, -3.06 kcal/mol), consistent with π electrons interacting with the C–S σ antibonding orbital. A fourth pattern places MSM above the ring with a perpendicular orientation, where one C–S bond aligns antiparallel to the ring dipole (*struc_2*, -4.43 kcal/mol). Geometries featuring C–H \cdots S contacts are also observed (*struc_3*, -3.21 kcal/mol), reflecting weak hydrogen-bond donation from aromatic C–H groups to sulfur lone pairs. Collectively, these motifs underscore how

methionine-like sulfur can engage aromatics through directional stereoelectronic and electrostatic complementarity, providing structural principles relevant to stereospecific recognition in Met-containing binding environments.

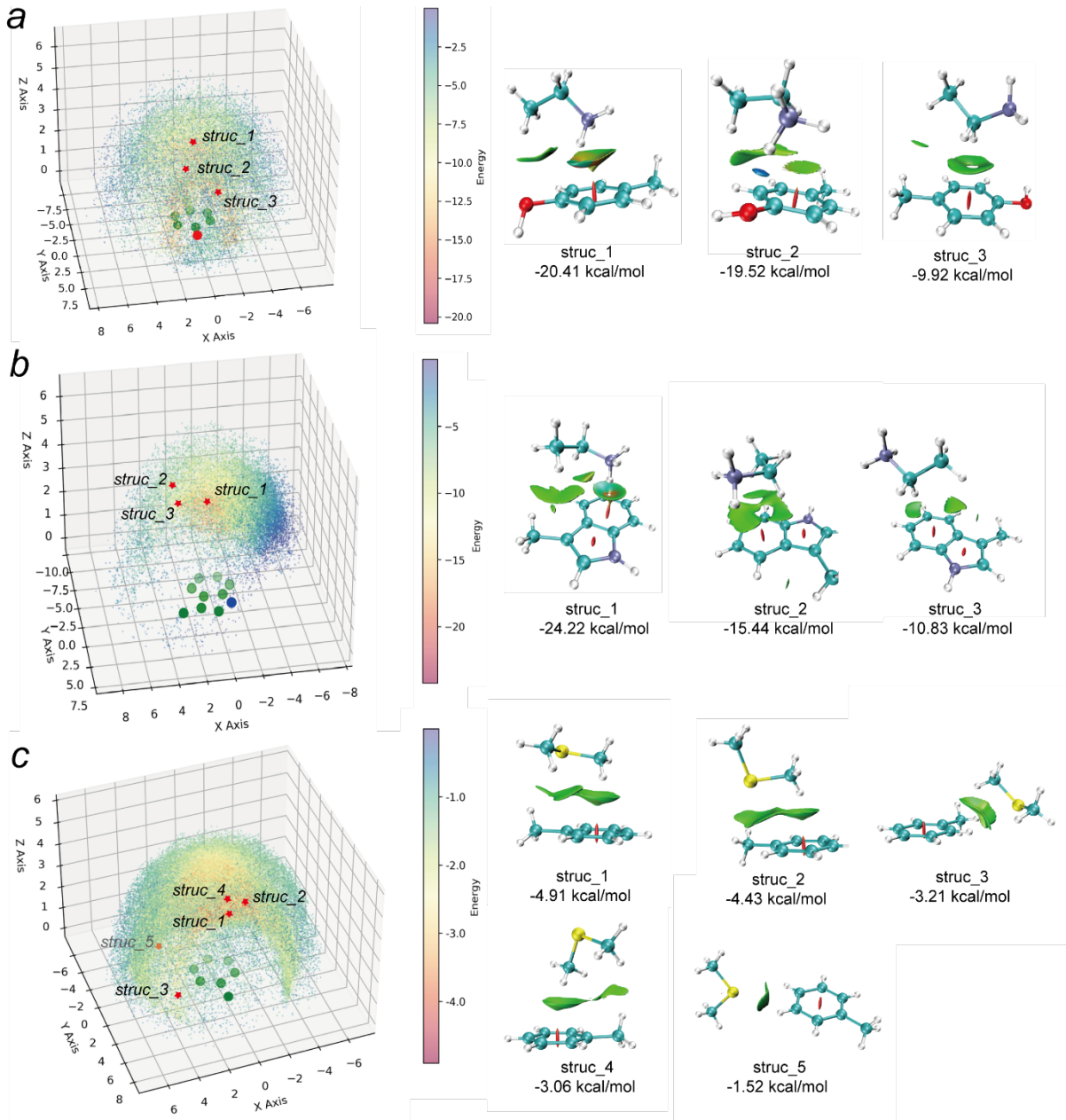


Figure 4. Spatial distribution and representative low-energy structure of ETAM-PMPO (a), ETAM-MIND (b), and MBZ-MSM (c) dimers. In the left column, each scatter point represents the position of the fragment's central atom (N or S) relative to the central fragment. The color of each scatter point corresponds to the energy scale shown in the adjacent color bar. Circles on the xy-plane represent heavy atoms of the central fragment: green for carbon atoms, red for oxygen atoms, and blue for nitrogen. Red stars mark the positions of the structures shown in the right column. The right column depicts the lowest-energy structures representing characteristic interaction patterns for each dimer. Isosurfaces show NCI maps between the fragments, and the NCI energy of each structure is given below the corresponding image.

Application to Protein-Ligand Complexes. To demonstrate the potential application in biomolecular modeling, PANIP was applied as a fragment-based scoring function for protein-ligand docking on three model systems: (1) indole bound to the apolar L99A mutant (PDB: 185L)⁴⁵, (2) phenol bound to the polar L99A/M102H double mutant (PDB: 4I7L)⁴⁶, and (3) serine bound to pyruvate kinase M2 (PKM2, PDB: 4B2D)⁴⁷ (Figure 5). The interaction energies ΔE_{bind} of all docking poses were calculated using both our PANIP scoring function (Eq.4) and the united AMBER force field energy function in DOCK. Pose prediction accuracy was quantified via root mean square deviation (RMSD) of ligand heavy atoms relative to crystallographic poses (Table 1). Native poses extracted from crystal structures were included in the docking pool for validation.

Across these systems, PANIP substantially improved pose ranking relative to an AMBER-based docking score. In L99A-indole, PANIP ranked the native pose first among 500 docking poses, while DOCK score selected a pose with an RMSD of 0.34 Å (ranked No. 160; Figure 5a,

b). In L99A/M102H-phenol, PANIP identified the native pose (No. 1), outperforming DOCK (No. 76; RMSD 0.21 Å; Figure 5c, d). In PKM2-serine, the serine ligand was decomposed into fragments (ACET, ETAM, and ETOH) for binding energy estimation. PANIP ranked the native pose third (RMSD 0.44 Å), while DOCK ranked it No. 46 (RMSD 1.29 Å). The top PANIP pose features a hydrogen bond (2.321 Å) between ligand serine's hydroxyl group and the carbonyl group of ILE469, differing from the native pose (2.149 Å; OH → ARG43 C=O; Figure 5e). However, the top PANIP-selected pose positioned the serine hydroxyl group near the serine NH₃⁺ fragment, potentially inducing intramolecular repulsion not captured by the pairwise fragment approximation, illustrating a key limitation of the current framework.

Table 1. Binding pose prediction for three protein targets: L99A (PDB 185L) in complex with indole; L99A/M102H in complex with phenol (PDB 1LI2); PKM2 in complex with serine (PDB 4B2D) with PANIP and AMBER. The native pose is the pose in the crystal structure. The best prediction is the best pose predicted by different scoring functions.

Ligand	Protein	PDB ID	Ranking of Native Pose (500 poses)		RMSD of the best prediction (Å)	
			PANIP	DOCK	PANIP	DOCK
Indole	L99A	185L	1	160	0.10	0.34
Phenol	L99A/M102H	4I7L	1	76	0.18	0.21
Serine	PKM2	4B2D	3	46	0.44	1.29

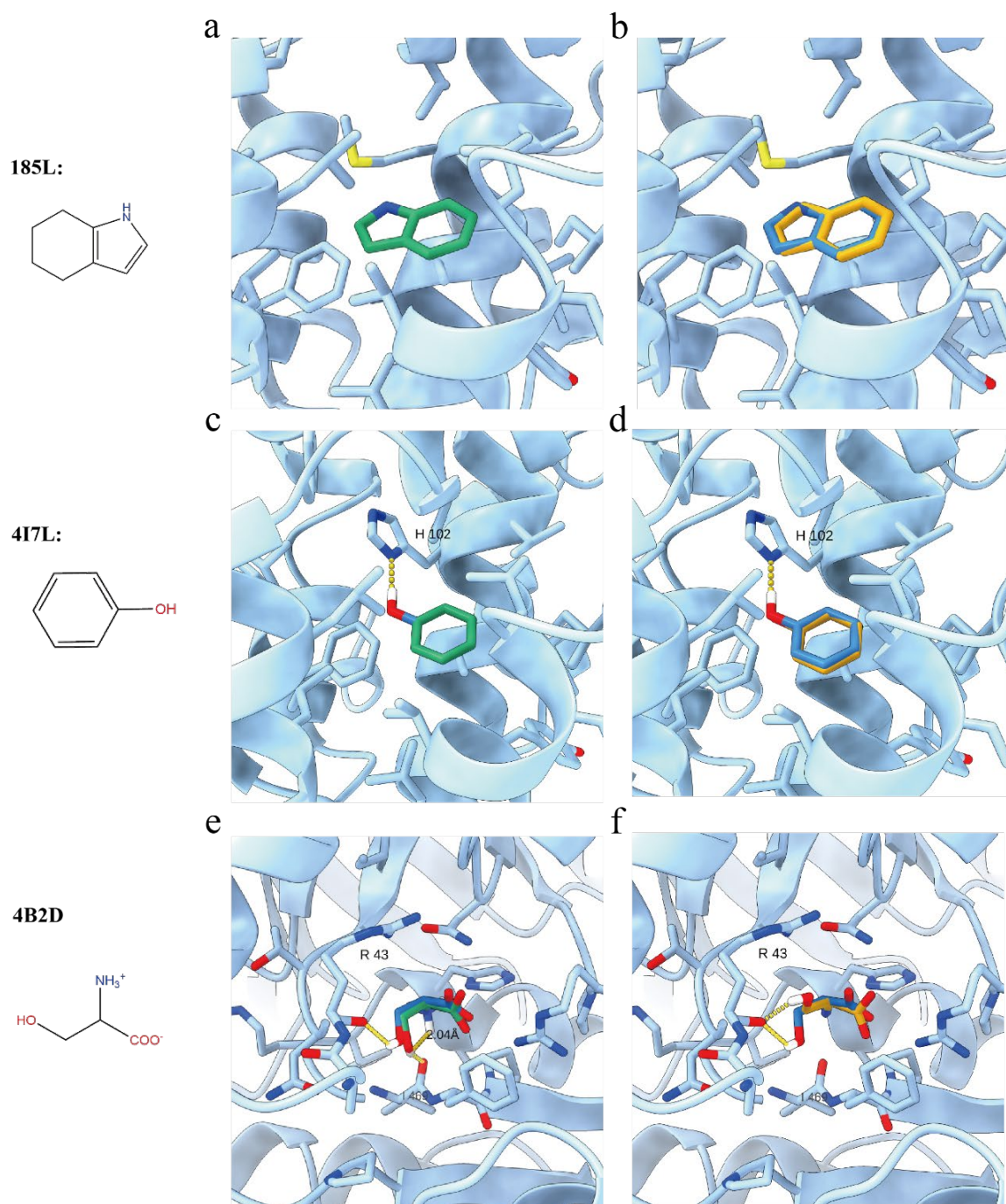


Figure 5. Structures and the best binding pose of indole ligand in L99A (top), phenol ligand in L99A/M102H (middle), and serine in PKM2 (bottom) predicted by our scoring function (green) and AMBER (yellow). The native structures are colored in blue for comparison. Structures are visualized in ChimeraX⁷⁶.

Additional model systems were evaluated (Table 2), including various alkyl-substituted benzene isomers and phenol binding to L99A and its polar or charged variants (L99A/M102Q, M102H, and M102E), as well as amino acid ligands such as alanine and phenylalanine interacting with PKM2. Across these systems, PANIP-based scoring function achieved a 44% native pose recovery rate (ranked first) across 25 model systems, consistently outperformed the DOCK score in recovering native poses and reducing RMSDs of top-ranked structures. Notably, this performance is achieved without explicit long-range electrostatic or solvation corrections, suggesting that accurate short-range NCI energetics are a dominant factor for pose discrimination in these relatively simple model systems.

Table 2. Binding pose prediction for three protein targets: L99, L99A/M102Q, and PKM2 with PANIP and DOCK. The native pose is the pose in the crystal structure. The best prediction is the best pose predicted by different scoring functions*.

Ligand	PDB ID	Ranking of Native Pose (500 poses)		RMSD of the best prediction (Å)	
		PANIP	DOCK	PANIP	DOCK
L99A					
toluene	4W53	82	128	0.29	0.41
isobutylbenzene	184L	1	271	0.37	0.91
n-Butylbenzene	4W57	1	34	1.36	1.38
benzene	181L	95	490	0.93	0.83
benzene	3HH4	40	250	0.11	0.64
benzene	4W52	57	273	0.06	0.67
ethylbenzene	4W54	1	500+	1.47	1.57
ethylbenzene	3HH6	2	250	0.28	0.50

propylbenzene	4W55	33	500+	0.26	0.39
sec-butylbenzene	4W56	1	11	0.99	1.07
octylbenzene	4W59	58	231	2.004	2.01
p-toluene	187L	95	470	0.55	0.58
<hr/>					
L99A/M102Q					
<hr/>					
benzene	5JWT	71	197	0.23	0.59
ethylbenzene	5JWV	1	198	0.68	0.91
phenol	1LI2	64	69	0.27	0.15
<hr/>					
L99A/M102H					
<hr/>					
benzene	4I7J	33	323	0.48	0.50
toluene	4I7K	37	284	0.33	0.64
<hr/>					
L99A/M102E					
<hr/>					
benzene	3GUJ	1	269	0.20	0.39
toluene	3GUK	1	223	1.46	0.65
ethylbenzene	3GUL	6	95	0.22	0.36
<hr/>					
PKM2					
<hr/>					
alanine	2G50	9	30	0.71	0.71
phenylalanine	4FXJ	1	1	0.43	0.45

* For structures exhibiting alternative conformations, the scoring results correspond to the conformation with the highest occupancy value.

DISCUSSION

We present PANIP, a protein-specific MLIP for NCIs, trained on PDB-derived fragment dimers with ω B97X-D3BJ/def2-TZVPP reference energies. A multi-fidelity active learning workflow enabled the construction of PDB-FRAGID, a high-precision, low-redundancy dataset

that compresses 36.3 million dimers to \sim 3.15 million representative structures while preserving the diversity of 17 fragment types and 153 dimer combinations. PANIP achieves sub-chemical-accuracy MAEs across multiple benchmark sets, generalizes to CSD-derived and non-equilibrium geometries, and offers near force-field computational cost, making it suitable for large-scale exploration of protein NCI landscapes.

Compared to the widely used ANI-2x potential, PANIP delivers markedly lower errors on protein-derived fragments, especially for charged and strongly interacting dimers, underscoring the value of targeted, high-fidelity NCI training data. When integrated into a fragment-based energy decomposition scheme, PANIP serves as an effective scoring function for protein–ligand docking, outperforming an AMBER-based score in pose ranking for a range of model systems. While the current framework focuses on pairwise interactions, ongoing efforts aim to expand fragment diversity to cover broader chemical spaces, to incorporate long-range electrostatic, multi-body, and solvation effects. Strategies include integrating well-established force field correction terms^{48,49}, leveraging ML-based correction schemes^{50,51}, or employing metamodeling approaches⁵². Together, PDB-FRAGID and PANIP provide a foundation for scalable, QM-accurate modeling of protein NCIs and for refining both data-driven and classical force-field descriptions in biomolecular simulations.

METHODS

Overall Workflow. As illustrated in Figure 6, a systematic workflow was developed to build MLIPs that leverage chemically relevant fragment–fragment interactions derived from high-resolution protein structures in the PDB. Proteins were fragmented into dimeric pairs to generate

an initial dataset, which was first labeled with baseline interaction energies computed at the low-cost r2SCAN-3c level²⁸. An MFAL method was designed to iteratively guide the selection of a representative and diverse subset of dimers, ensuring balanced coverage of the full structural distribution. This refined subset, termed the PDB-FRAGID, was recalculated at the higher-accuracy ω B97X-D3BJ/def2-TZVPP level^{29,30}. The curated data was then used to train the PANIP models, resulting in robust MLIPs with QM level accuracy in predicting molecular interaction energies.

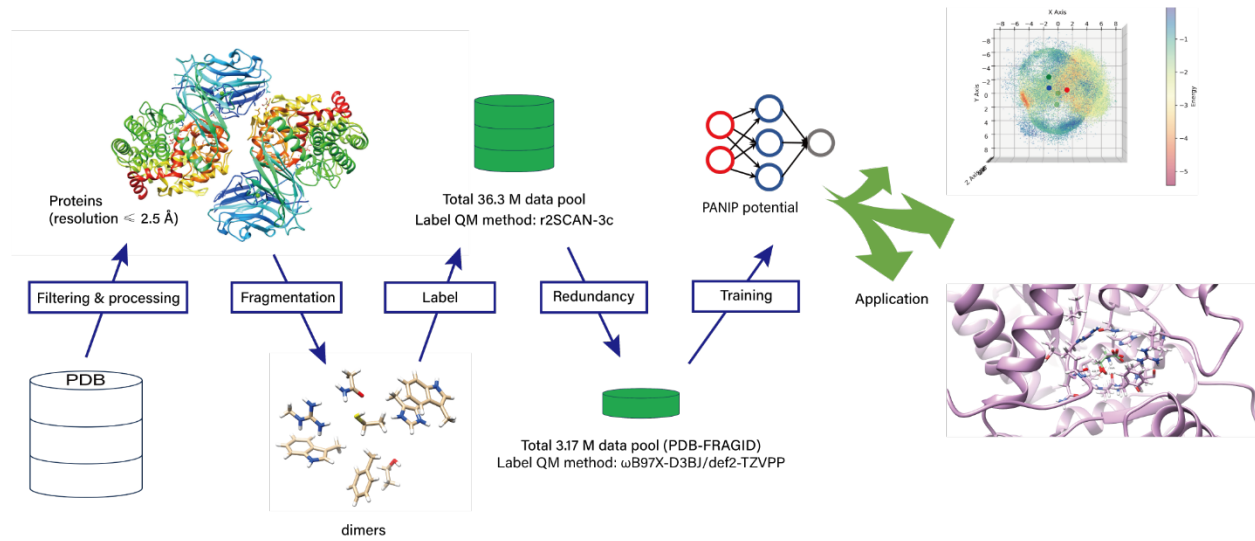


Figure 6. Overall workflow of dataset construction and model training.

Fragmentation Definition and Dimer Extraction. To represent NCIs in proteins, 17 chemically distinct fragment types were defined, encompassing amino acid side chains, backbone segment, and water (Figure 7). Key atoms (e.g., carbons bonded to aromatic rings, thiols, hydroxyls, or ammonium groups) were retained to preserve local electronic environments and minimize symmetry-related redundancy. These fragments were paired into 153 unique dimer types, forming the basis for NCI analysis.

Initial protein structures were obtained from PDB entries with resolution ≤ 2.5 Å and unique UniProt⁵³ IDs to reduce redundancy, yielding 29,204 proteins. Missing hydrogens were added using the high-throughput molecular dynamics (HTMD) approach⁵⁴, while the original PDB coordinates were preserved without further structural optimization. Protonation states of ionizable residues were assigned according to typical physiological conditions: all three common protonation states were considered for histidine, reflecting its pKa near physiological pH, whereas lysine and arginine side chains were treated as protonated, and aspartic acid side chains as deprotonated.

Interacting fragment pairs were identified using two criteria. First, the shortest heavy-atom distances between 2 and 4 Å (capturing interactions slightly beyond the sum of van der Waals radii for atomic pairs (C=1.70 Å, N=1.55 Å, O=1.52 Å, S=1.80 Å) and excluding covalent bonds (<2 Å)⁵⁵). The 4 Å upper bound was chosen to focus on geometries where NCIs are most significant, while avoiding an overwhelming number of weak, long-range contacts. Second, fragment pairs were required to be separated by at least two residues along the protein sequence to mitigate trivial local contacts arising from backbone connectivity. This yielded a raw set of 36.3 million dimers spanning 153 unique fragment-fragment combinations across the 17 fragment types in protein (see Supporting Information for details).

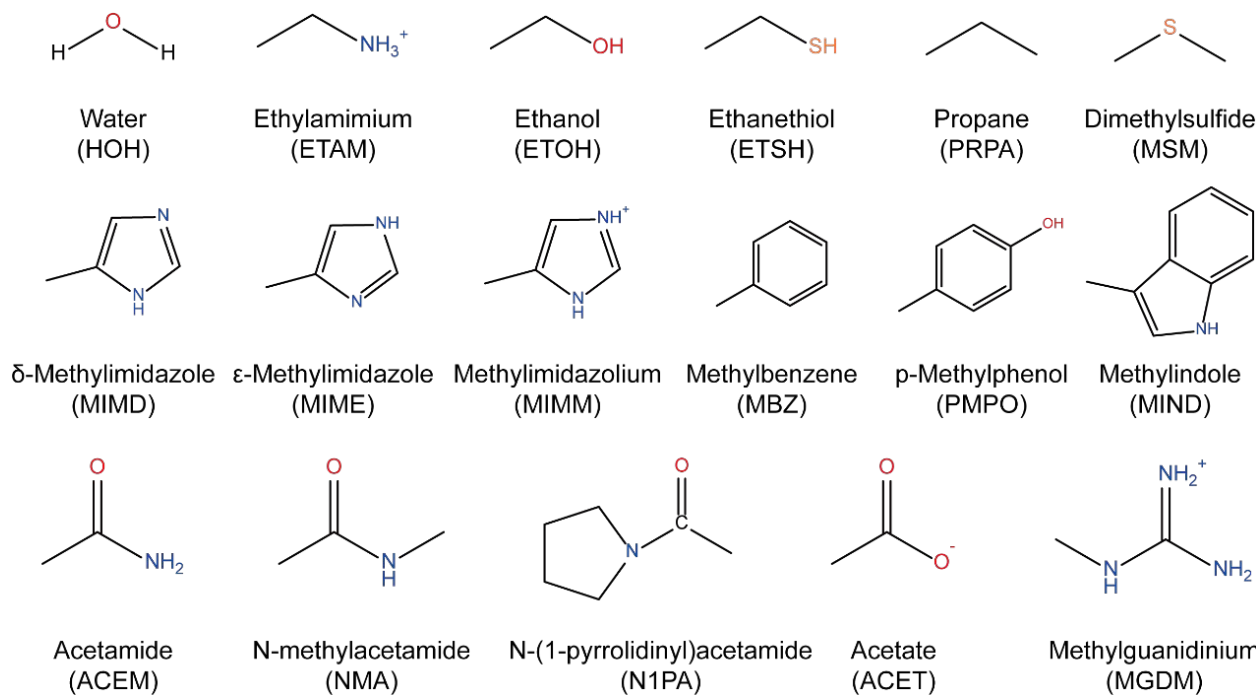


Figure 7.17 17 representative chemical groups defined in proteins.

Data Reduction via Multi-Fidelity Active Learning. To balance computational efficiency with accuracy, a multi-fidelity active learning workflow^{26,27} was designed (Figure S1). MFAL extends active learning by combining low-cost quantum chemical approximations with selected high-fidelity refinements, reducing the need for exhaustive expensive calculations. Specifically, the r²SCAN-3c method²⁸ served as a low-fidelity oracle to provide baseline interaction energies for all dimers. r²SCAN-3c combines the r²SCAN meta-GGA functional with atom-pairwise dispersion and basis-set corrections, and was calculated using ORCA 5.0.3⁵⁶. The non-covalent interaction energy (ΔE_{AB}) for each dimer was computed as:

$$\Delta E_{AB} = E(AB) - [E(A) + E(B)] \quad (1)$$

where $E(AB)$, $E(A)$, and $E(B)$ represent the total energy of the dimer and isolated monomers, respectively.

As an initial step, a 2% random bootstrap set was used to train an initial surrogate model based on NequIP³¹. The surrogate model was then iteratively applied to the remaining dimers, and an uncertainty-based acquisition function flagged high-error cases using the normalized criterion $|E_{pred} - E_{ref}|/\sqrt{N} > 0.04$ kcal/mol, where E_{pred} is the predicted energy, E_{ref} is the reference (r²SCAN-3c) energy, and N is the atom count. In each iteration, a random 2% subset of these flagged structures was added to the training set. This iterative loop continued until fewer than 5% of the unscreened dimers remained as high-error cases, which were then fully included in the final dataset. The final refined subset (PDB-FRAGID) condensed the original pool to a representative core comprising only 8.7% of its size (~3.15 million) while preserving balanced coverage of the full structural distribution.

High-Level QM labeling. All dimers in the PDB-FRAGID dataset were recomputed at the higher-accuracy ω B97X-D3BJ/def2-TZVPP level^{29,30} using ORCA 5.0.3⁵⁶. The ω B97X-D3BJ²⁹ (a range-separated hybrid meta-GGA density functional with D3(BJ) empirical dispersion correction) coupled with the def2-TZVPP³⁰ basis set delivers exceptional precision for modeling non-covalent interactions and conformational energies while maintaining a balanced treatment of short- and long-range electronic correlations^{29,30}. The resolution of identity approximation with coulomb, exchange, and correlation contributions (RIJCOSX) approximation⁵⁷ was applied to accelerate calculations, with auxiliary basis sets def2/J⁵⁸ and def2-TZVPP/C⁵⁹ employed for integration and correlation treatments. The ma-def2-TZVPP⁶⁰ diffuse function was added only for negatively charged oxygen atoms (e.g., in carboxylate groups like ACET) to improve electron density descriptions. For neutral systems, additional diffuse functions provided no benefit and could even introduce numerical instabilities. The basis set superposition error (BSSE)

was corrected using the counterpoise method⁶¹⁻⁶³. NCI energies were computed according to Eq.1.

These high-fidelity ω B97X-D3BJ/def2-TZVPP interaction energies on PDB-FRAGID serve as the reference data for training PANIP.

Training Protocol of PANIP. PANIP was implemented as an ensemble of NequIP³¹, an equivariant graph neural network that explicitly encodes the rotational, translational, and permutational symmetries of atomistic systems. By enforcing E(3)-equivariance in its message-passing layers, NequIP achieves high data efficiency and systematically improved accuracy compared to conventional invariant graph neural networks. This makes it particularly well-suited for learning NCI energies, where capturing subtle orientation-dependent non-covalent effects is essential. For NequIP training, we modified the default settings as follows: a cutoff radius of 7.5 Å, inclusion of O, N, and S in the chemical symbols list, and a batch size of 512. Early stopping was applied with a patience of 100 epochs on the validation loss. Global energy rescaling was set to *dataset_total_energy_std* (the standard deviation of total energies in the dataset).

To accelerate the construction of the final model, MFAL-selected subsets from each fragment type were first used to train fragment-specific NequIP models. These fragment-wise datasets were then combined to form the unified PDB-FRAGID dataset, which was used to train the final PANIP ensemble (5 models) via five-fold cross-validation. Unless otherwise noted, predictions are reported as ensemble averages. In addition, fragment-specific models generally exhibit slightly higher accuracy on their respective subsets but reduced generalization across fragment types, whereas the unified PANIP model provides robust performance across the full diversity of protein-derived NCIs. Full training protocols, hyperparameters, and model files are available on GitHub (<https://github.com/hnlab/PANIP>).

Benchmark Datasets. PANIP was evaluated on four benchmark sets derived from both protein and non-protein sources. First, the low-energy representative from the original r²SCAN-3c-labeled pool was selected for each unique dimer type, resulting in 277 candidate structures. These structures were optimized at the r²SCAN-3c level to ensure well-defined equilibrium geometries, forming a dedicated benchmark set. Single-point energy calculations were performed using the ω B97X-D3BJ/def2-TZVPP method on all selected dimer geometries (with and without optimization). This benchmark set was used to assess model performance in reproducing equilibrium interaction energies. Same-charge dimer pairs were excluded due to frequent wave function convergence failures during optimization.

Second, to evaluate model transferability beyond training data, dimers involving the same fragment types were extracted from CSD³² using ConQuest⁶⁴. Although the chemical fragment pairs are identical, the geometries originate from small-molecule structures (not protein environments) and thus sample distinct conformational and packing motifs — providing a complementary test of generalization across structural sources. To preserve structural integrity and chemical independence, only dimers featuring single aliphatic bonds (C-C or C-H) were retained. Pairs with the closest interatomic distances between 2 and 4 Å were selected, aligning with NCI criteria established for PDB dimers. Organometallic structures were excluded and hydrogen positions were normalized to standard bond geometries, yielding 33,274 CSD-derived dimers for analysis.

Third, to evaluate performance on non-equilibrium conformations, a biased fragment-pair random sampling method was developed. Fragments were treated as rigid bodies with fixed bond lengths and angles. Initial 3D fragment structures were generated from SMILES strings⁶⁵ using the RDKit software package⁶⁶. One fragment was fixed at the origin, and the other was

positioned within a 12 Å radius sphere centered on the fixed fragment, with rotational sampling applied. A biased random sampling protocol was implemented using a logarithmic normal distribution for the acceptance probability:

$$x = r_i^{vdw} + r_j^{vdw} - d_{ij} \quad (2)$$

$$p(x) = \frac{1}{(-x+c)\sigma\sqrt{2\pi}} e^{-\frac{(\ln(-x+c)-\mu)^2}{2\sigma^2}} \quad (3)$$

Where x is the intermolecular overlap (Å), r_i^{vdw} and r_j^{vdw} are the van der Waals radii of atoms i and j , and d_{ij} is their interatomic distance. Parameters were set to $\sigma=0.8$, $\mu=1.0$, and $c=1.6$ —chosen to maximize acceptance probability at an intermolecular overlap of ~0.1 Å (favoring physically realistic conformations) and ensure overlaps remained below 1.6 Å to avoid severe clashes^{67,68} (Figure S2). This coordinate system enabled denser sampling at shorter intermolecular distances and sparser sampling at longer distances. For each dimer type, 100 conformations were sampled, yielding a total of 15,300 conformations. Interaction energies for these dimers were computed using both PANIP and ωB97X-D3BJ/def2-TZVPP for comparison.

Finally, to benchmark against an established ML potential, the ANI-2x neural network potential⁹ (a widely used model trained on large organic molecule datasets, covering C, H, O, N, and S elements) was employed to predict NCI energies of the CSD subset for comparison with PANIP. The pre-trained ANI-2x neural networks are available in TorchANI python library⁶⁹. Since ANI-2x predicts total energies, NCI energies were calculated by applying Eq. 1 to the ANI-2x predicted total energies of the dimer and its corresponding monomers. Because ANI-2x was not parameterized for charged systems, performance was evaluated both on datasets

including and excluding charged dimers, with detailed results provided in the Supporting Information.

Docking and Rescoring. We evaluated the model ensemble’s ability to predict the native-like binding pose for three protein-ligand model systems^{70,71}: L99A in complex with indole (PDB 185L)⁴⁵, L99A/M102H in complex with phenol (PDB 4I7L)⁴⁶, and the M2 isoform of pyruvate kinase (PKM2) in complex with serine (PDB 4B2D)⁷². Docking was performed using default parameter settings from an automated platform as described previously^{73,74}. For all docking poses generated by DOCK 3.7⁷⁵, binding energies were first calculated using scoring functions based on the united AMBER force field (as in DOCK 3.7).

To compute binding interaction energies with PANIP, both the receptor and ligand were fragmented within a 5 Å distance cutoff around the ligand (Figure 8). Notably, for PKM2-serine, the serine ligand was decomposed into three fragments (ACET, ETAM, and ETOH). The PANIP-estimated binding interaction energy is given by

$$\Delta E_{bind} = \sum_i^{rec} \sum_j^{lig} \Delta E_{pred} + \Delta E_{lnk} - \Delta E_{dup} \quad (4)$$

where ΔE_{pred} is the interaction energy between protein fragment i and ligand fragment j (computed using PANIP), ΔE_{lnk} accounts for energy contributions from linking atoms (protein/ligand, green circle in Figure 8), and ΔE_{dup} corrects for double-counted atoms in fragment-fragment interactions (orange circle in Figure 8).

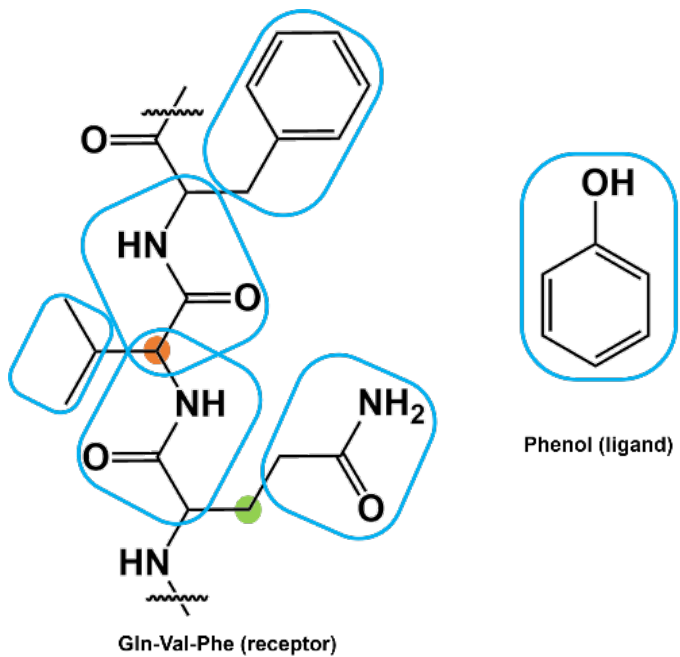


Figure 8. The sketch of protein fragmentation approach. Receptor and ligand are decomposed into fragments (blue boxes), linker atoms (green circle), and duplicated atoms (orange circle)

DATA AVAILABILITY

PDB-FRAGID can be downloaded from Zenodo (<https://zenodo.org/records/18213106>). The trained models of PANIP, benchmark sets used in this paper are available for download from a GitHub repository <https://github.com/hnlab/PANIP>. The PDB-FRAGID dataset is available at <https://github.com/hnlab/PDB-FRAGID>.

CODE AVAILABILITY

Related codes are publicly available at <https://github.com/hnlab/PANIP>.

AUTHOR INFORMATION

Corresponding Author

*E-mail: huangniu@nibs.ac.cn

ORCID

Niu Huang: 0000-0002-6912-033X

Lejia Zeng: 0009-0004-3410-8404

Funding Sources

Beijing Municipal Science and Technology Commission, Administrative Commission of Zhongguancun Science Park, Grant/Award Number: Z201100005320012

Notes

The authors declare no competing financial interest.

ACKNOWLEDGMENT

This work is supported by Beijing Municipal Science & Technology Commission (Z201100005320012 to Niu Huang) and Tsinghua University.

ABBREVIATIONS

AL, active learning; BSSE, basis set superposition; CSD, Cambridge Structural Database; HTMD, high-throughput molecular dynamics; MAE, mean absolute error; MLIPS, machine learning interatomic potentials; ML, machine learning; NCIs, non-covalent interactions; NequIP, Neural Equivariant Interatomic Potentials; PDB, Protein Data Bank; PDB-FRAGID, PDB Fragment Interaction Dataset; PES, potential energy surfaces; PKM2, M2 isoform of pyruvate kinase; RMSD, root mean square deviation; QM, quantum mechanical.

REFERENCES

- (1) Han, Y.; Ali, I.; Wang, Z.; Cai, J.; Wu, S.; Tang, J.; Zhang, L.; Ren, J.; Xiao, R.; Lu, Q.; Hang, L.; Luo, H.; Li, J. Machine Learning Accelerates Quantum Mechanics Predictions of Molecular Crystals. *Physics Reports* 2021, 934, 1–71.
<https://doi.org/10.1016/j.physrep.2021.08.002>.
- (2) Dral, P. O. Quantum Chemistry in the Age of Machine Learning. *J. Phys. Chem. Lett.* 2020, 11 (6), 2336–2347. <https://doi.org/10.1021/acs.jpclett.9b03664>.
- (3) Behler, J. Four Generations of High-Dimensional Neural Network Potentials. *Chem. Rev.* 2021, 121 (16), 10037–10072. <https://doi.org/10.1021/acs.chemrev.0c00868>.
- (4) von Lilienfeld, O. A.; Müller, K.-R.; Tkatchenko, A. Exploring Chemical Compound Space with Quantum-Based Machine Learning. *Nat Rev Chem* 2020, 4 (7), 347–358.
<https://doi.org/10.1038/s41570-020-0189-9>.

(5) Behler, J.; Csányi, G. Machine Learning Potentials for Extended Systems: A Perspective. *Eur. Phys. J. B* 2021, 94 (7), 142. <https://doi.org/10.1140/epjb/s10051-021-00156-1>.

(6) Combining Machine Learning and Computational Chemistry for Predictive Insights Into Chemical Systems | Chemical Reviews. <https://pubs.acs.org/doi/10.1021/acs.chemrev.1c00107> (accessed 2025-01-06).

(7) Gastegger, M.; Behler, J.; Marquetand, P. Machine Learning Molecular Dynamics for the Simulation of Infrared Spectra. *Chem. Sci.* 2017, 8 (10), 6924–6935. <https://doi.org/10.1039/C7SC02267K>.

(8) Donchev, A. G.; Taube, A. G.; Decolvenaere, E.; Hargus, C.; McGibbon, R. T.; Law, K.-H.; Gregersen, B. A.; Li, J.-L.; Palmo, K.; Siva, K.; Bergdorf, M.; Klepeis, J. L.; Shaw, D. E. Quantum Chemical Benchmark Databases of Gold-Standard Dimer Interaction Energies. *Sci Data* 2021, 8 (1), 55. <https://doi.org/10.1038/s41597-021-00833-x>.

(9) Devereux, C.; Smith, J. S.; Huddleston, K. K.; Barros, K.; Zubatyuk, R.; Isayev, O.; Roitberg, A. E. Extending the Applicability of the ANI Deep Learning Molecular Potential to Sulfur and Halogens. *J. Chem. Theory Comput.* 2020, 16 (7), 4192–4202. <https://doi.org/10.1021/acs.jctc.0c00121>.

(10) Qiao, Z.; Welborn, M.; Anandkumar, A.; Manby, F. R.; Miller, T. F., III. OrbNet: Deep Learning for Quantum Chemistry Using Symmetry-Adapted Atomic-Orbital Features. *The Journal of Chemical Physics* 2020, 153 (12), 124111. <https://doi.org/10.1063/5.0021955>.

(11) Ullah, A.; Dral, P. O. Molecular Quantum Chemical Data Sets and Databases for Machine Learning Potentials. *ChemRxiv* August 21, 2024. <https://doi.org/10.26434/chemrxiv-2024-w3ld0>.

(12) Řezáč, J. Non-Covalent Interactions Atlas Benchmark Data Sets: Hydrogen Bonding. *ChemRxiv* December 19, 2019. <https://doi.org/10.26434/chemrxiv.11365040.v1>.

(13) Eastman, P.; Behara, P. K.; Dotson, D. L.; Galvelis, R.; Herr, J. E.; Horton, J. T.; Mao, Y.; Chodera, J. D.; Pritchard, B. P.; Wang, Y.; De Fabritiis, G.; Markland, T. E. SPICE, A Dataset of Drug-like Molecules and Peptides for Training Machine Learning Potentials. *Sci Data* 2023, 10 (1), 11. <https://doi.org/10.1038/s41597-022-01882-6>.

(14) Jurečka, P.; Šponer, J.; Černý, J.; Hobza, P. Benchmark Database of Accurate (MP2 and CCSD(T) Complete Basis Set Limit) Interaction Energies of Small Model Complexes, DNA Base Pairs, and Amino Acid Pairs. *Phys. Chem. Chem. Phys.* 2006, 8 (17), 1985–1993. <https://doi.org/10.1039/B600027D>.

(15) A Perspective on Deep Learning for Molecular Modeling and Simulations. <https://doi.org/10.1021/acs.jpca.0c04473>.

(16) Ko, T. W.; Finkler, J. A.; Goedecker, S.; Behler, J. Accurate Fourth-Generation Machine Learning Potentials by Electrostatic Embedding. *J. Chem. Theory Comput.* 2023, 19 (12), 3567–3579. <https://doi.org/10.1021/acs.jctc.2c01146>.

(17) Kocer, E.; Ko, T. W.; Behler, J. Neural Network Potentials: A Concise Overview of Methods. *Annual Review of Physical Chemistry* 2022, 73 (Volume 73, 2022), 163–186. <https://doi.org/10.1146/annurev-physchem-082720-034254>.

(18) Eastman, P.; Pritchard, B. P.; Chodera, J. D.; Markland, T. E. Nutmeg and SPICE: Models and Data for Biomolecular Machine Learning. *J. Chem. Theory Comput.* 2024, 20 (19), 8583–8593. <https://doi.org/10.1021/acs.jctc.4c00794>.

(19) Levine, D. S.; Shuaibi, M.; Spotte-Smith, E. W. C.; Taylor, M. G.; Hasyim, M. R.; Michel, K.; Batatia, I.; Csányi, G.; Dzamba, M.; Eastman, P.; Frey, N. C.; Fu, X.; Gharakhanyan, V.; Krishnapriyan, A. S.; Rackers, J. A.; Raja, S.; Rizvi, A.; Rosen, A. S.; Ulissi, Z.; Vargas, S.; Zitnick, C. L.; Blau, S. M.; Wood, B. M. The Open Molecules 2025 (OMol25) Dataset, Evaluations, and Models. *arXiv* May 13, 2025. <https://doi.org/10.48550/arXiv.2505.08762>.

(20) Wood, B. M.; Dzamba, M.; Fu, X.; Gao, M.; Shuaibi, M.; Barroso-Luque, L.; Abdelmaqsoud, K.; Gharakhanyan, V.; Kitchin, J. R.; Levine, D. S.; Michel, K.; Sriram, A.; Cohen, T.; Das, A.; Rizvi, A.; Sahoo, S. J.; Ulissi, Z. W.; Zitnick, C. L. UMA: A Family of Universal Models for Atoms. *arXiv* June 30, 2025. <https://doi.org/10.48550/arXiv.2506.23971>.

(21) Berman, H. M.; Westbrook, J.; Feng, Z.; Gilliland, G.; Bhat, T. N.; Weissig, H.; Shindyalov, I. N.; Bourne, P. E. The Protein Data Bank. *Nucleic Acids Research* 2000, 28 (1), 235–242. <https://doi.org/10.1093/nar/28.1.235>.

(22) Ferreira de Freitas, R.; Schapira, M. A Systematic Analysis of Atomic Protein–Ligand Interactions in the PDB. *Med. Chem. Commun.* 2017, 8 (10), 1970–1981. <https://doi.org/10.1039/C7MD00381A>.

(23) Burra, P. V.; Zhang, Y.; Godzik, A.; Stec, B. Global Distribution of Conformational States Derived from Redundant Models in the PDB Points to Non-Uniqueness of the Protein

Structure. *Proceedings of the National Academy of Sciences* 2009, 106 (26), 10505–10510.

<https://doi.org/10.1073/pnas.0812152106>.

(24) Kirchmair, J.; Markt, P.; Distinto, S.; Schuster, D.; Spitzer, G. M.; Liedl, K. R.; Langer, T.; Wolber, G. The Protein Data Bank (PDB), Its Related Services and Software Tools as Key Components for In Silico Guided Drug Discovery. *J. Med. Chem.* 2008, 51 (22), 7021–7040.

<https://doi.org/10.1021/jm8005977>.

(25) Bank, R. P. D. PDB Statistics: Overall Growth of Released Structures Per Year.

<https://www.rcsb.org/stats/growth/growth-released-structures> (accessed 2025-01-21).

(26) Hernandez-Garcia, A.; Saxena, N.; Jain, M.; Liu, C.-H.; Bengio, Y. Multi-Fidelity Active Learning with GFlowNets. *arXiv* September 1, 2024. <https://doi.org/10.48550/arXiv.2306.11715>.

(27) Peherstorfer, B.; Willcox, K.; Gunzburger, M. Survey of Multifidelity Methods in Uncertainty Propagation, Inference, and Optimization. *SIAM Rev.* 2018, 60 (3), 550–591.

<https://doi.org/10.1137/16M1082469>.

(28) Grimme, S.; Hansen, A.; Ehlert, S.; Mewes, J.-M. r2SCAN-3c: A “Swiss Army Knife” Composite Electronic-Structure Method. *J. Chem. Phys.* 2021, 154 (6), 064103.

<https://doi.org/10.1063/5.0040021>.

(29) Chai, J.-D.; Head-Gordon, M. Long-Range Corrected Hybrid Density Functionals with Damped Atom–Atom Dispersion Corrections. *Phys. Chem. Chem. Phys.* 2008, 10 (44), 6615–6620. <https://doi.org/10.1039/B810189B>.

(30) Grimme, S.; Ehrlich, S.; Goerigk, L. Effect of the Damping Function in Dispersion Corrected Density Functional Theory. *Journal of Computational Chemistry* 2011, 32 (7), 1456–1465. <https://doi.org/10.1002/jcc.21759>.

(31) Batzner, S.; Musaelian, A.; Sun, L.; Geiger, M.; Mailoa, J. P.; Kornbluth, M.; Molinari, N.; Smidt, T. E.; Kozinsky, B. E(3)-Equivariant Graph Neural Networks for Data-Efficient and Accurate Interatomic Potentials. *Nat Commun* 2022, 13 (1), 2453. <https://doi.org/10.1038/s41467-022-29939-5>.

(32) Groom, C. R.; Bruno, I. J.; Lightfoot, M. P.; Ward, S. C. The Cambridge Structural Database. *Acta Cryst B* 2016, 72 (2), 171–179. <https://doi.org/10.1107/S2052520616003954>.

(33) Law, R.; Barker, O.; Barker, J. J.; Hesterkamp, T.; Godemann, R.; Andersen, O.; Fryatt, T.; Courtney, S.; Hallett, D.; Whittaker, M. The Multiple Roles of Computational Chemistry in Fragment-Based Drug Design. *J Comput Aided Mol Des* 2009, 23 (8), 459–473. <https://doi.org/10.1007/s10822-009-9284-1>.

(34) Priya Gnanasekar, S.; Arunan, E. Molecular Beam and Spectroscopic Techniques: Towards Fundamental Understanding of Intermolecular Interactions/Bonds. 2017. <https://doi.org/10.1039/BK9781782621737-00259>.

(35) Vioglio, P. C.; Chierotti, M. R.; Gobetto, R. Solid-State NMR Techniques for the Study of Intermolecular Interactions.

(36) Devereux, C.; Smith, J. S.; Huddleston, K. K.; Barros, K.; Zubatyuk, R.; Isayev, O.; Roitberg, A. E. Extending the Applicability of the ANI Deep Learning Molecular Potential to

Sulfur and Halogens. *J. Chem. Theory Comput.* 2020, 16 (7), 4192–4202.
<https://doi.org/10.1021/acs.jctc.0c00121>.

(37) Lu, T.; Chen, Q. Visualization Analysis of Weak Interactions in Chemical Systems. In *Comprehensive Computational Chemistry* (First Edition); Yáñez, M., Boyd, R. J., Eds.; Elsevier: Oxford, 2024; pp 240–264. <https://doi.org/10.1016/B978-0-12-821978-2.00076-3>.

(38) Dougherty, D. A. Cation-Pi Interactions Involving Aromatic Amino Acids. *J Nutr* 2007, 137 (6 Suppl 1), 1504S-1508S; discussion 1516S-1517S. <https://doi.org/10.1093/jn/137.6.1504S>.

(39) Infield, D. T.; Rasouli, A.; Galles, G. D.; Chipot, C.; Tajkhorshid, E.; Ahern, C. A. Cation- π Interactions and Their Functional Roles in Membrane Proteins. *Journal of Molecular Biology* 2021, 433 (17), 167035. <https://doi.org/10.1016/j.jmb.2021.167035>.

(40) Gallivan, J. P.; Dougherty, D. A. Cation- π Interactions in Structural Biology. *Proceedings of the National Academy of Sciences* 1999, 96 (17), 9459–9464.
<https://doi.org/10.1073/pnas.96.17.9459>.

(41) Wu, R.; McMahon, T. B. Investigation of Cation- π Interactions in Biological Systems. *J. Am. Chem. Soc.* 2008, 130 (38), 12554–12555. <https://doi.org/10.1021/ja802117s>.

(42) Ma, J. C.; Dougherty, D. A. The Cation- π Interaction. *Chem. Rev.* 1997, 97 (5), 1303–1324. <https://doi.org/10.1021/cr9603744>.

(43) Pal, D.; Chakrabarti, P. Non-Hydrogen Bond Interactions Involving the Methionine Sulfur Atom. *Journal of Biomolecular Structure and Dynamics* 2001, 19 (1), 115–128.
<https://doi.org/10.1080/07391102.2001.10506725>.

(44) Allen, F. H.; Bird, C. M.; Rowland, R. S.; Raithby, P. R. Resonance-Induced Hydrogen Bonding at Sulfur Acceptors in R1R2C=S and R1CS2– Systems. *Acta Crystallographica Section B* 1997, 53 (4), 680–695. <https://doi.org/10.1107/S0108768197002656>.

(45) Morton, A.; Matthews, B. W. Specificity of Ligand Binding in a Buried Nonpolar Cavity of T4 Lysozyme: Linkage of Dynamics and Structural Plasticity. *Biochemistry* 1995, 34 (27), 8576–8588. <https://doi.org/10.1021/bi00027a007>.

(46) Merski, M.; Shoichet, B. K. The Impact of Introducing a Histidine into an Apolar Cavity Site on Docking and Ligand Recognition. *J Med Chem* 2013, 56 (7), 2874–2884. <https://doi.org/10.1021/jm301823g>.

(47) Serine is a natural ligand and allosteric activator of pyruvate kinase M2 | *Nature*. <https://www.nature.com/articles/nature11540> (accessed 2025-01-15).

(48) Páll, S.; Zhmurov, A.; Bauer, P.; Abraham, M.; Lundborg, M.; Gray, A.; Hess, B.; Lindahl, E. Heterogeneous Parallelization and Acceleration of Molecular Dynamics Simulations in GROMACS. *The Journal of Chemical Physics* 2020, 153 (13), 134110. <https://doi.org/10.1063/5.0018516>.

(49) Thompson, A. P.; Aktulga, H. M.; Berger, R.; Bolintineanu, D. S.; Brown, W. M.; Crozier, P. S.; in 't Veld, P. J.; Kohlmeyer, A.; Moore, S. G.; Nguyen, T. D.; Shan, R.; Stevens, M. J.; Tranchida, J.; Trott, C.; Plimpton, S. J. LAMMPS - a Flexible Simulation Tool for Particle-Based Materials Modeling at the Atomic, Meso, and Continuum Scales. *Computer Physics Communications* 2022, 271, 108171. <https://doi.org/10.1016/j.cpc.2021.108171>.

(50) Grumet, M.; von Scarpatetti, C.; Bučko, T.; Egger, D. A. Delta Machine Learning for Predicting Dielectric Properties and Raman Spectra. *J. Phys. Chem. C* 2024, 128 (15), 6464–6470. <https://doi.org/10.1021/acs.jpcc.4c00886>.

(51) Nováček, M.; Řezáč, J. PM6-ML: The Synergy of Semiempirical Quantum Chemistry and Machine Learning Transformed into a Practical Computational Method. December 6, 2024. <https://doi.org/10.26434/chemrxiv-2024-3nwwv-v3>.

(52) Learning together: Towards foundation models for machine learning interatomic potentials with meta-learning | *npj Computational Materials*. <https://www.nature.com/articles/s41524-024-01339-x> (accessed 2025-03-13).

(53) The UniProt Consortium. UniProt: A Worldwide Hub of Protein Knowledge. *Nucleic Acids Research* 2019, 47 (D1), D506–D515. <https://doi.org/10.1093/nar/gky1049>.

(54) Doerr, S.; Harvey, M. J.; Noé, F.; De Fabritiis, G. HTMD: High-Throughput Molecular Dynamics for Molecular Discovery. *J. Chem. Theory Comput.* 2016, 12 (4), 1845–1852. <https://doi.org/10.1021/acs.jctc.6b00049>.

(55) Smith, J. G.; McGraw-Hill Companies. *Organic Chemistry*; McGraw-Hill Education, 2016.

(56) Neese, F. The ORCA Program System. *WIREs Computational Molecular Science* 2012, 2 (1), 73–78. <https://doi.org/10.1002/wcms.81>.

(57) Neese, F.; Wennmohs, F.; Hansen, A.; Becker, U. Efficient, Approximate and Parallel Hartree–Fock and Hybrid DFT Calculations. A ‘Chain-of-Spheres’ Algorithm for the Hartree–

Fock Exchange. *Chemical Physics* 2009, 356 (1), 98–109.

<https://doi.org/10.1016/j.chemphys.2008.10.036>.

(58) Weigend, F. Accurate Coulomb-Fitting Basis Sets for H to Rn. *Phys. Chem. Chem. Phys.* 2006, 8 (9), 1057–1065. <https://doi.org/10.1039/B515623H>.

(59) Hill, J. G.; Platts, J. A. Auxiliary Basis Sets for Density-Fitted MP2 Calculations: Correlation-Consistent Basis Sets for the 4d Elements. *J. Chem. Theory Comput.* 2009, 5 (3), 500–505. <https://doi.org/10.1021/ct8005584>.

(60) Zheng, J.; Xu, X.; Truhlar, D. G. Minimally Augmented Karlsruhe Basis Sets. *Theor Chem Acc* 2011, 128 (3), 295–305. <https://doi.org/10.1007/s00214-010-0846-z>.

(61) Boys, S. F.; Bernardi, F. The Calculation of Small Molecular Interactions by the Differences of Separate Total Energies. Some Procedures with Reduced Errors. *Molecular Physics* 1970, 19 (4), 553–566. <https://doi.org/10.1080/00268977000101561>.

(62) Simon, S.; Duran, M.; Dannenberg, J. J. How Does Basis Set Superposition Error Change the Potential Surfaces for Hydrogen-bonded Dimers? *The Journal of Chemical Physics* 1996, 105 (24), 11024–11031. <https://doi.org/10.1063/1.472902>.

(63) van Duijneveldt, F. B.; van Duijneveldt-van de Rijdt, J. G. C. M.; van Lenthe, J. H. State of the Art in Counterpoise Theory. *Chem. Rev.* 1994, 94 (7), 1873–1885.
<https://doi.org/10.1021/cr00031a007>.

(64) Bruno, I. J.; Cole, J. C.; Edgington, P. R.; Kessler, M.; Macrae, C. F.; McCabe, P.; Pearson, J.; Taylor, R. New Software for Searching the Cambridge Structural Database and

Visualizing Crystal Structures. *Acta Cryst B* 2002, 58 (3), 389–397.

<https://doi.org/10.1107/S0108768102003324>.

(65) Weininger, D. SMILES, a Chemical Language and Information System. 1. Introduction to Methodology and Encoding Rules. *J. Chem. Inf. Comput. Sci.* 1988, 28 (1), 31–36.

<https://doi.org/10.1021/ci00057a005>.

(66) RDKit. <http://www.rdkit.org/> (accessed 2023-05-23).

(67) Limpert, E.; Stahel, W. A.; Abbt, M. Log-Normal Distributions across the Sciences: Keys and Clues: On the Charms of Statistics, and How Mechanical Models Resembling Gambling Machines Offer a Link to a Handy Way to Characterize Log-Normal Distributions, Which Can Provide Deeper Insight into Variability and Probability—Normal or Log-Normal: That Is the Question. *BioScience* 2001, 51 (5), 341–352. [https://doi.org/10.1641/0006-3568\(2001\)051%255B0341:LNDATS%255D2.0.CO;2](https://doi.org/10.1641/0006-3568(2001)051%255B0341:LNDATS%255D2.0.CO;2).

(68) Pettersen, E. F.; Goddard, T. D.; Huang, C. C.; Couch, G. S.; Greenblatt, D. M.; Meng, E. C.; Ferrin, T. E. UCSF Chimera--a Visualization System for Exploratory Research and Analysis. *J Comput Chem* 2004, 25 (13), 1605–1612. <https://doi.org/10.1002/jcc.20084>.

(69) Gao, X.; Ramezanghorbani, F.; Isayev, O.; Smith, J. S.; Roitberg, A. E. TorchANI: A Free and Open Source PyTorch Based Deep Learning Implementation of the ANI Neural Network Potentials. 24.

(70) Wei, B. Q.; Baase, W. A.; Weaver, L. H.; Matthews, B. W.; Shoichet, B. K. A Model Binding Site for Testing Scoring Functions in Molecular Docking. *J Mol Biol* 2002, 322 (2), 339–355. [https://doi.org/10.1016/s0022-2836\(02\)00777-5](https://doi.org/10.1016/s0022-2836(02)00777-5).

(71) Li, Y.; Bao, M.; Yang, C.; Chen, J.; Zhou, S.; Sun, R.; Wu, C.; Li, X.; Bao, J. Computer-Aided Identification of a Novel Pyruvate Kinase M2 Activator Compound. *Cell Proliferation* 2018, 51 (6), e12509. <https://doi.org/10.1111/cpr.12509>.

(72) Chaneton, B.; Hillmann, P.; Zheng, L.; Martin, A. C. L.; Maddocks, O. D. K.; Chokkathukalam, A.; Coyle, J. E.; Jankevics, A.; Holding, F. P.; Vousden, K. H.; Frezza, C.; O'Reilly, M.; Gottlieb, E. Serine Is a Natural Ligand and Allosteric Activator of Pyruvate Kinase M2. *Nature* 2012, 491 (7424), 458–462. <https://doi.org/10.1038/nature11540>.

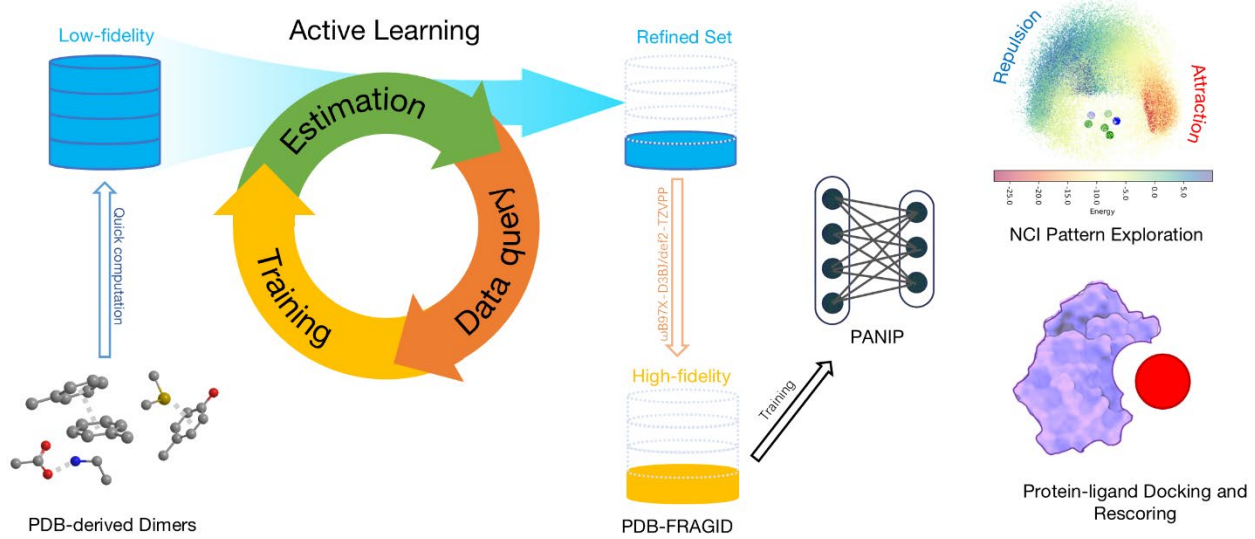
(73) Huang, N.; Shoichet, B. K.; Irwin, J. J. Benchmarking Sets for Molecular Docking. *J. Med. Chem.* 2006, 49 (23), 6789–6801. <https://doi.org/10.1021/jm0608356>.

(74) Irwin, J. J.; Shoichet, B. K.; Mysinger, M. M.; Huang, N.; Colizzi, F.; Wassam, P.; Cao, Y. Automated Docking Screens: A Feasibility Study. *J. Med. Chem.* 2009, 52 (18), 5712–5720. <https://doi.org/10.1021/jm9006966>.

(75) Meng, E. C.; Shoichet, B. K.; Kuntz, I. D. Automated Docking with Grid-Based Energy Evaluation. *Journal of Computational Chemistry* 1992, 13 (4), 505–524. <https://doi.org/10.1002/jcc.540130412>.

(76) Pettersen, E. F.; Goddard, T. D.; Huang, C. C.; Meng, E. C.; Couch, G. S.; Croll, T. I.; Morris, J. H.; Ferrin, T. E. UCSF ChimeraX: Structure Visualization for Researchers, Educators, and Developers. *Protein Science* 2021, 30 (1), 70–82. <https://doi.org/10.1002/pro.3943>.

TOC Graphic



Robust MLIPs that achieve accuracy comparable to the ω B97X-D3BJ/def2-TZVPP level on non-covalent interactions.

Supporting Information for Developing a Machine Learning Interatomic Potential for Non- Covalent Interactions in Proteins

Lejia Zeng^{1,2}, Xintong Zhang^{1,2}, Yuchan Pei^{1,2}, Lifeng Zhao², Lan Hua², Jincai Yang², Niu

Huang^{1,2,}*

¹Tsinghua Institute of Multidisciplinary Biomedical Research, Tsinghua University, Beijing
102206, China

²National Institute of Biological Sciences, 7 Science Park Road, Zhongguancun Life Science
Park, Beijing 102206, China

E-mail: huangniu@nibs.ac.cn

Contents

1	Dimer Extraction.....	3
2	Active Learning Workflow.....	4
3	Random Sampling.....	5
4	Accuracy and Efficiency Benchmark.....	6
5	Exploring NCI patterns in PDB.....	8
6	Supporting Information Tables.....	9
	References.....	12

1 Dimer Extraction

Dimers were extracted from protein structures using an in-house script. For each type of fragment, a corresponding SMARTS¹ pattern was generated, and SMILES² patterns were also employed to define the three-dimensional templates. Substructure searches across all collected proteins were then carried out through SMARTS-based substructure matching implemented in RDKit³ Python package. The coordinates of matching atoms of each hit were mapped onto the template atoms defined by corresponding SMILES patterns. When isolation of the fragment required cleavage of a C–C or C–N bond, the bond was cut at the appropriate position, the resulting terminal atom was first marked as a dummy atom, and then capped with hydrogen to maintain valency.

Once 17 chemical groups had been collected from a given protein, dimers were searched for by identifying fragment pairs in close spatial proximity. Each interacting pair was initially labeled as the shortest distance between 2 and 4 Å. And the residue in which two fragments are located should be separated by at least 2 amino acids to avoid bias from proximity effects.

2 Active Learning Workflow

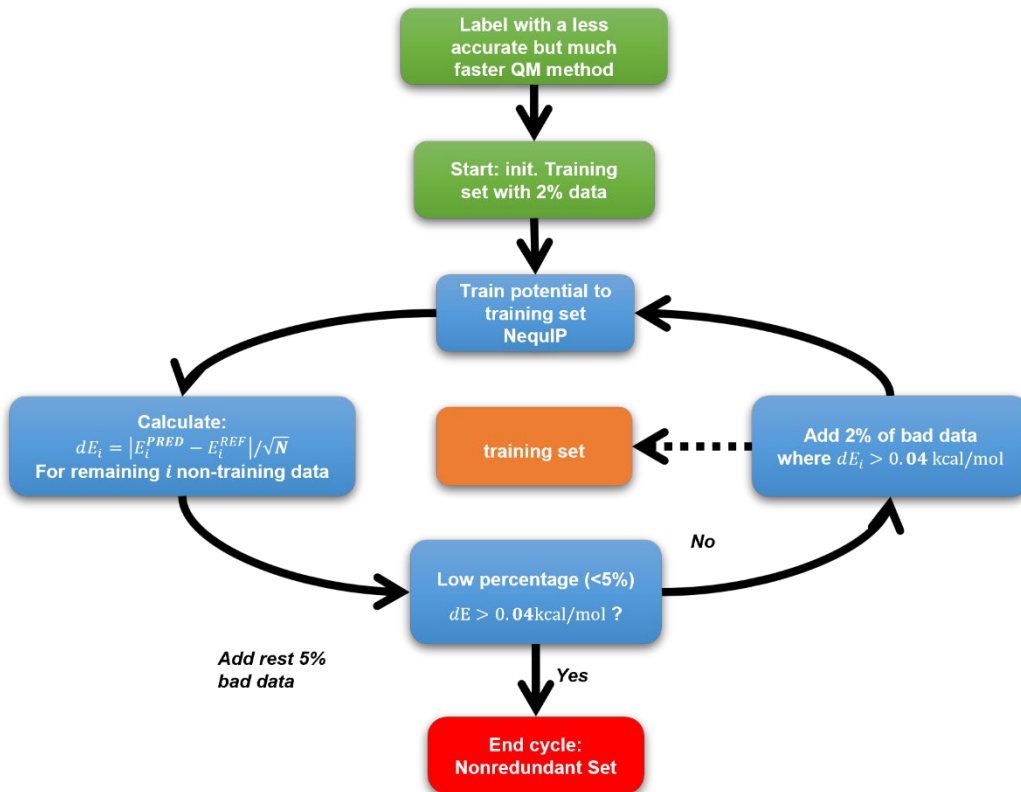


Figure S1. AL workflow for data redundancy.

3 Random Sampling

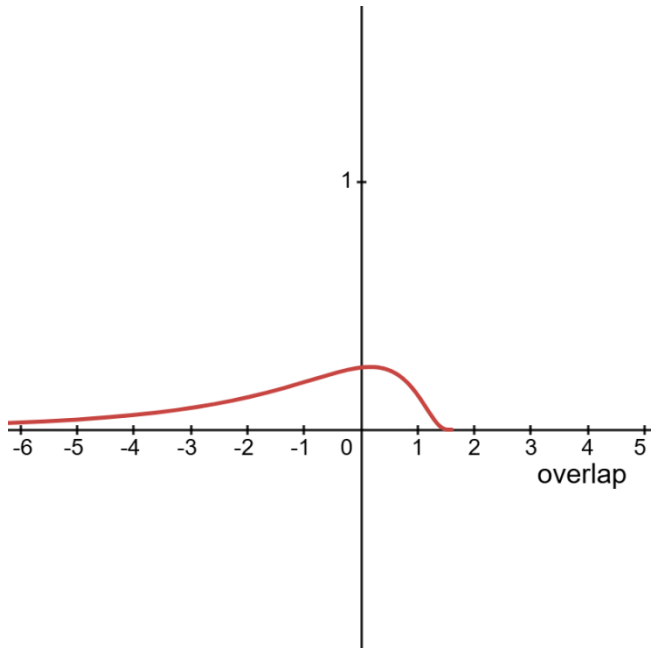


Figure S2. Acceptance probability curve for intermolecular overlap used in random sampling.

Curve visualization generated via <https://www.desmos.com/calculator/a8imk7uszg>.

4 Model Performance on Benchmark Sets

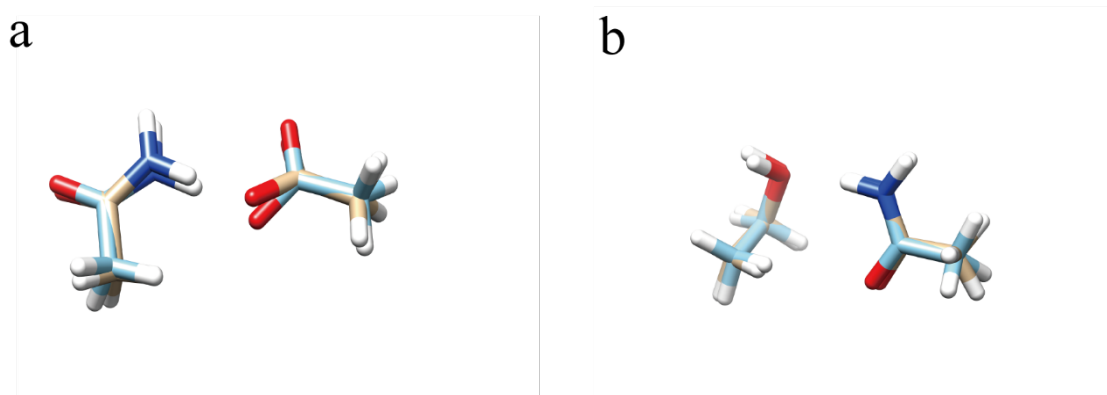


Figure S3. Conformational changes observed in post-optimization. Initial lowest-energy structures (tan) and their optimized counterparts (sky blue) exhibit minimal structural deviations, as quantified by root-mean-square deviation (RMSD) values of (a) 0.399 Å for ACEM-ACET and (b) 0.352 Å for ACEM-ETOH.

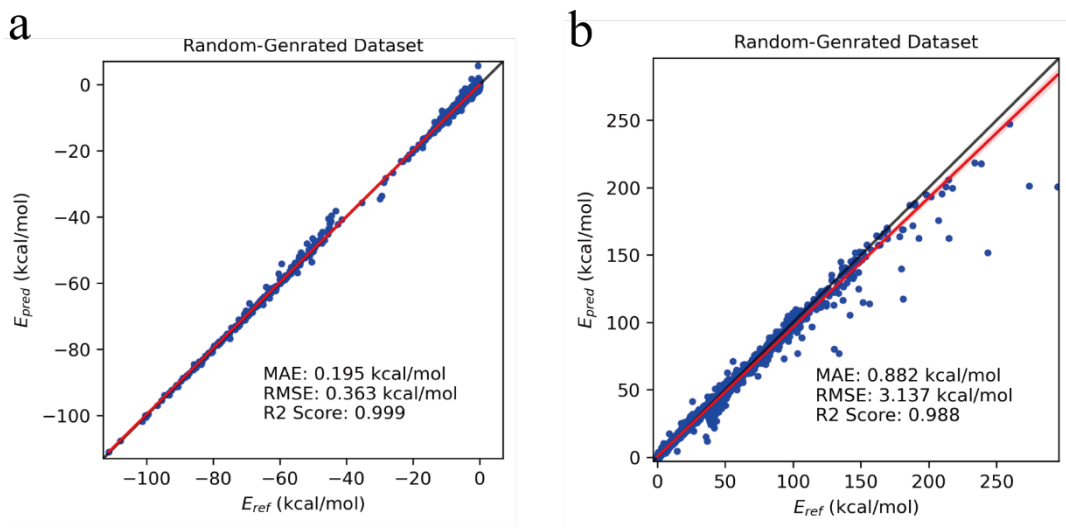


Figure S4. Interaction energies calculated at ω B97X-D3BJ/def2-TZVPP level and predicted by PANIP for samples with energy (a) below 0 kcal/mol and (b) above 0 kcal/mol in random-generated dataset. The black line indicates perfect prediction ($y = x$), and the red line shows the regression fit.

5 Comparison with ANI-2x

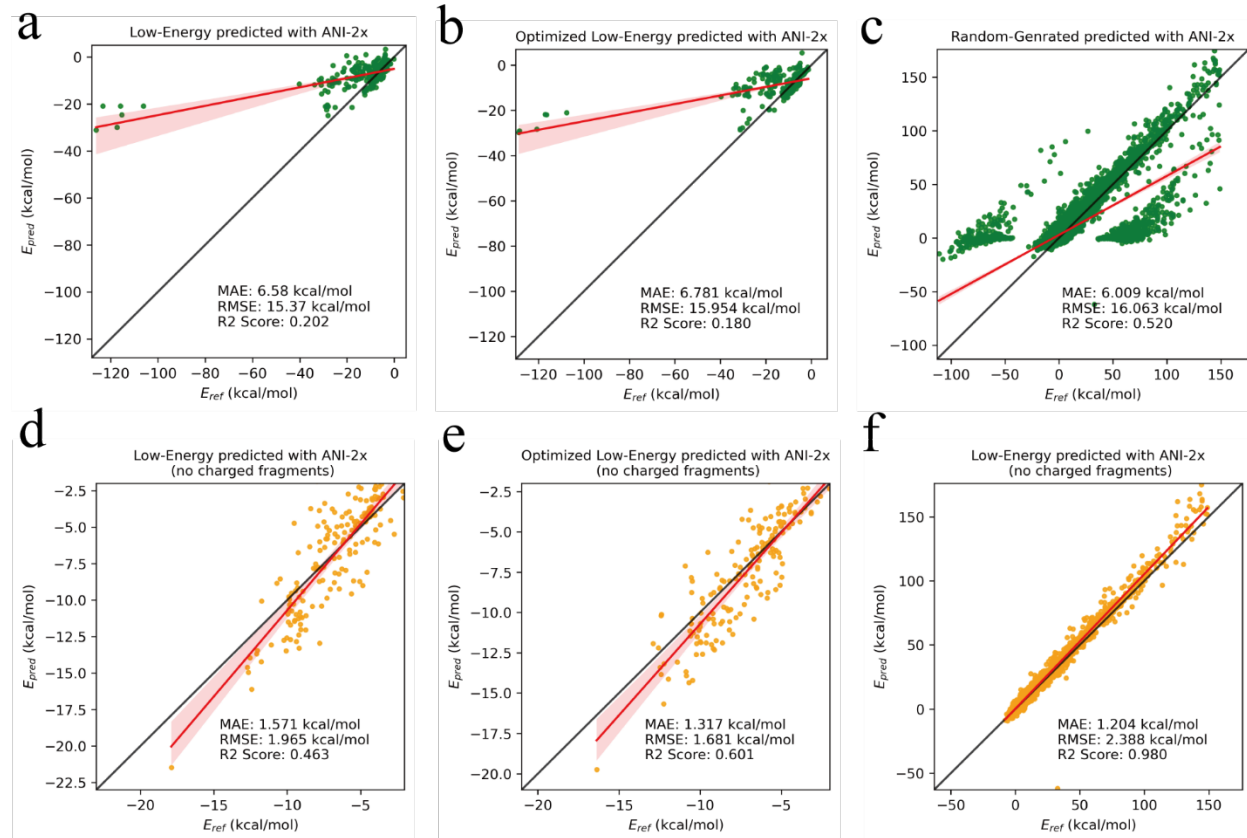


Figure S5. Correlation plots between non-covalent interaction energies calculated at ω B97X-D3BJ/def2-TZVPP level, E_{ref} , and predicted by ANI-2x, E_{pred} , for low-energy dataset (a, d), optimized low-energy dataset (b, e), and random-generated dataset (c, f). Panels a–c include all samples; panels d–f exclude dimers containing charged fragments.

6 Exploring NCI Patterns in PDB

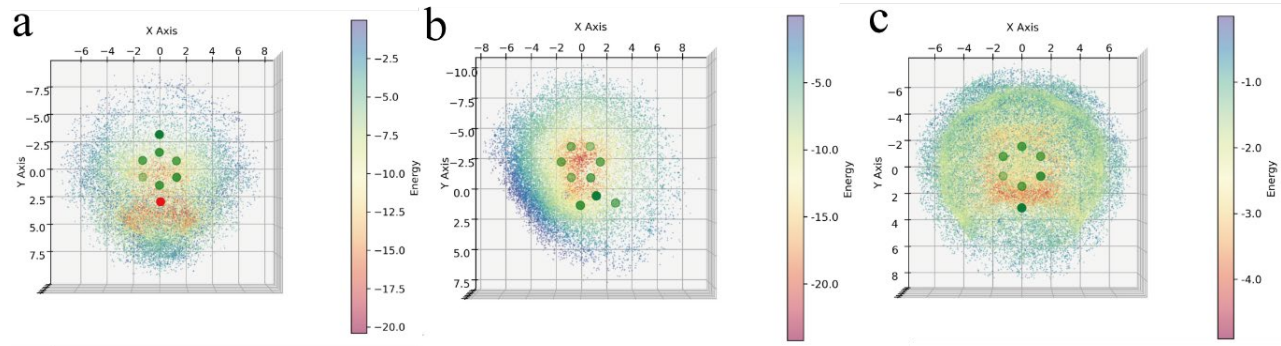


Figure S6. Bottom view of spatial distributions for ETAM-PMPO (a), ETAM-MIND (b), and MBZ-MSM (c). Each scatter point represents the position of the fragment's central atom (N or S) relative to the central fragment. The color of each scatter point corresponds to the energy scale shown in the adjacent color bar. Circles on the xy-plane represent heavy atoms of the central fragment: green for carbon atoms, red for oxygen atoms, and blue for nitrogen.

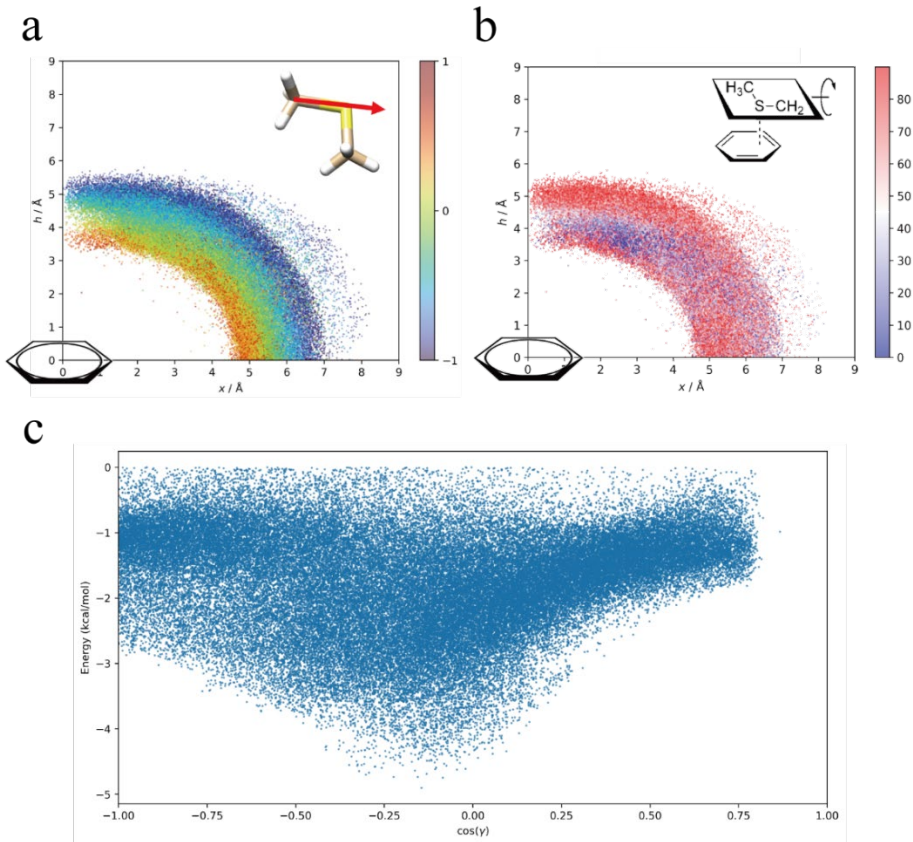


Figure S7. Radial distribution of MSM around aromatic rings, with x as the centroid shift (\AA) and h as the height above the plane (\AA), with point colors indicating the trend of the geometric parameter of interest. (a) Orientation distribution of the C→S vector. The color bar denotes orientation ($\cos\gamma$): values > 0 (red) correspond to the C→S vector pointing toward the ring center, whereas values < 0 (blue) indicate the opposite direction. The inset (upper right) is the schematic of the C-S bond definition. (b) Interplanar angle distribution between the plane of the MSM fragment and the aromatic ring plane. The inset (upper right) illustrates the definition of the MSM fragment plane used in the analysis. (c) Predicted interaction energies (kcal/mol) for MBZ-MSM as a function of the C-S bond orientation ($\cos\gamma$, where 1 = toward the aromatic ring, -1 = away, 0 = parallel).

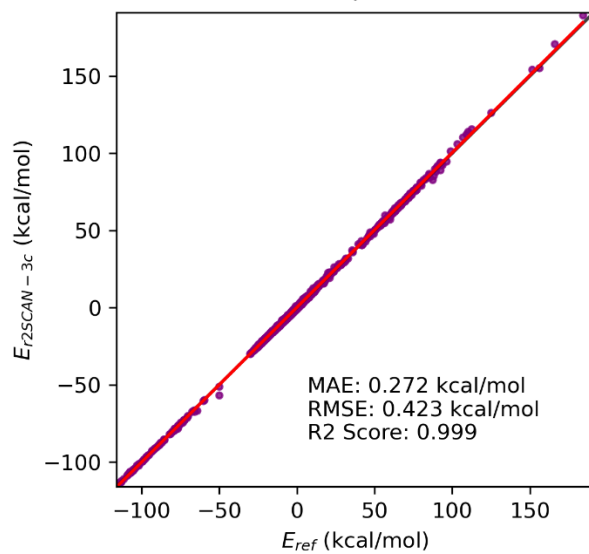


Figure S8. Comparison of interaction energies calculated at the ω B97X-D3BJ/def2-TZVPP level and r^2 SCAN-3c for randomly selected 30 dimers from each class.

7 NCI Visualization

The Reduced Density Gradient (RDG) method⁴ is used to visualize weak interactions. In this study, weak interaction analysis⁵ was performed using the Multiwfn program⁶, and the corresponding visualizations were generated with VMD software⁷. In the weak interaction analysis, the gradient isosurfaces of the RDG function are typically colored on a scale ranging from blue-green to red, corresponding to interaction strength from strong attraction to strong repulsion. Blue regions indicate strong attractive interactions, green regions correspond to weak van der Waals interactions, and red regions denote strong steric repulsion.

8 Supporting Information Tables

Table S1. Data volume of each fragment

Fragment type	Total number*	Training number**(%)***
ACEM	4,830,133	533,043 (11.03)
ACET	5,246,390	1,170,051 (22.30)
ETAM	1,480,001	347,779 (23.50)
ETOH	3,299,189	374,098 (11.34)
ETSH	350,411	79,419 (22.66)
MBZ	3,380,598	252,517 (7.47)
MGDM	2,520,733	474,908 (18.84)
Imidazole	1,377,566	284,607 (20.66)
MIND	1,325,598	194,941 (14.71)
PMPO	1,697,412	258,379 (15.22)
MSM	949,756	141,498 (14.90)
N1PA	1,103,276	179,516 (16.27)
NMA	22,026,093	876,434 (3.98)
PRPA	9,306,132	527,630 (5.67)
HOH	3,561,146	327,658 (9.20)

*The total number of occurrences in the original dataset.

**The number of occurrences in the training set.

***Percentage of total data used for training.

Table S2. Calculation time of each fragment

Fragment Type	Time*	
	(in hours)	PANIP
	ω B97X-D3BJ/def2-TZVPP	
ACEM	36 days, 20:03:14.2	0:39:18.0
ACET	20 days, 9:32:51.3	0:37:32.9
ETAM	45 days, 11:24:32.5	0:40:42.3
ETOH	34 days, 18:38:02.8	0:39:19.3
ETSH	29 days, 0:16:31.1	0:39:03.9
MBZ	53 days, 17:01:56.3	0:44:10.8
MGDM	66 days, 5:37:29.9	0:41:39.7
MIMD	56 days, 10:43:06.7	0:40:31.7
MIME	54 days, 12:43:22.4	0:41:42.3
MIMM	58 days, 13:51:29.8	0:40:60.0
MIND	108 days, 13:58:41.7	0:46:57.3
PMPO	80 days, 17:58:59.7	0:44:01.9
MSM	35 days, 0:20:00.7	0:39:58.2
N1PA	94 days, 2:16:00.9	0:46:23.8
NMA	47 days, 5:44:10.5	0:42:11.5
PRPA	36 days, 13:47:55.2	0:41:15.4
HOH	12 days, 21:28:45.8	0:35:22.9
Total	463 days, 11:19:06.1	6:17:55.6

*All benchmark calculations were performed on the computer cluster with an Intel Xeon Platinum 8368 CPU @ 2.60 GHz with 504 GB RAM.

REFERENCES

- (1) Daylight Theory: SMARTS - A Language for Describing Molecular Patterns.
<https://www.daylight.com/dayhtml/doc/theory/theory.smarts.html> (accessed 2023-05-23).
- (2) SMILES, a chemical language and information system. 1. Introduction to methodology and encoding rules | Journal of Chemical Information and Modeling.
<https://pubs.acs.org/doi/10.1021/ci00057a005> (accessed 2023-05-23).
- (3) RDKit. <http://www.rdkit.org/> (accessed 2023-05-23).
- (4) Johnson, E. R.; Keinan, S.; Mori-Sánchez, P.; Contreras-García, J.; Cohen, A. J.; Yang, W. Revealing Noncovalent Interactions. *J. Am. Chem. Soc.* 2010, 132 (18), 6498–6506.
<https://doi.org/10.1021/ja100936w>.
- (5) Lu, T.; Chen, Q. Visualization Analysis of Weak Interactions in Chemical Systems. In Comprehensive Computational Chemistry (First Edition); Yáñez, M., Boyd, R. J., Eds.; Elsevier: Oxford, 2024; pp 240–264. <https://doi.org/10.1016/B978-0-12-821978-2.00076-3>.
- (6) Lu, T.; Chen, F. Multiwfn: A Multifunctional Wavefunction Analyzer. *Journal of Computational Chemistry* 2012, 33 (5), 580–592. <https://doi.org/10.1002/jcc.22885>.
- (7) Humphrey, W.; Dalke, A.; Schulten, K. VMD: Visual Molecular Dynamics. *Journal of Molecular Graphics* 1996, 14 (1), 33–38. [https://doi.org/10.1016/0263-7855\(96\)00018-5](https://doi.org/10.1016/0263-7855(96)00018-5).